Exploiting many-body localization for scalable variational quantum simulation

Chenfeng Cao[1,2], Yeqing Zhou[3], Swamit Tannu[4], Nic Shannon[5], and Robert Joynt[3,6]

[1]HK Institute of Quantum Science & Technology, The University of Hong Kong, Hong Kong, China
[2]Dahlem Center for Complex Quantum Systems, Freie Universität Berlin, 14195 Berlin, Germany
[3]Department of Physics, University of Wisconsin-Madison, Madison, WI 53706, USA
[4]Department of Computer Science, University of Wisconsin-Madison, Madison, WI 53706, USA
[5]Theory of Quantum Matter Unit, Okinawa Institute of Science and Technology Graduate University, Onna-son, Okinawa 904-0412, Japan
[6]Theoretical Sciences Visiting Program (TSVP), Okinawa Institute of Science and Technology Graduate University, Onna, 904-0495, Japan

arXiv:2404.17560v6 [quant-ph] 25 Feb 2026

Variational quantum algorithms (VQAs) represent a promising pathway toward achieving practical quantum advantage on near-term hardware. Despite this promise, for generic, expressive ansätze, their scalability is critically hindered by barren plateaus—regimes of exponentially vanishing gradients. We demonstrate that initializing a hardware-efficient, Floquet-structured ansatz within the many-body localized (MBL) phase mitigates barren plateaus and enhances algorithmic trainability. Through analysis of the inverse participation ratio, entanglement entropy, and a novel low-weight stabilizer Rényi entropy, we characterize a distinct MBL–thermalization transition. Below a critical kick strength, the circuit avoids forming a unitary 2-design, exhibits robust area-law entanglement, and maintains non-vanishing gradients. Leveraging this MBL regime facilitates the efficient variational preparation of ground states for several model Hamiltonians with significantly reduced computational resources. Crucially, experiments on a 127-qubit superconducting processor provide evidence for the preservation of trainable gradients in the MBL phase for a kicked Heisenberg chain, validating our approach on contemporary noisy hardware. Our findings position MBL-based initialization as a viable strategy for developing scalable VQAs and motivate broader integration of localization into quantum algorithm design.

Chenfeng Cao: chenfeng.cao@connect.ust.hk

1 Introduction

Quantum computing promises to solve classically intractable problems in cryptography, optimization, and quantum chemistry. A key near-term approach is the variational quantum algorithm (VQA), a hybrid framework using parameterized quantum circuits and classical optimizers to mitigate hardware limits like coherence times and connectivity, tackling tasks like ground-state preparation via the Variational Quantum Eigensolver (VQE) for molecules [1, 2] or combinatorial optimization with the Quantum Approximate Optimization Algorithm (QAOA) [3, 4]. Nevertheless, scaling VQAs faces major challenges, most notably barren plateaus—exponential gradient decay with system size [5–9]. These arise from various sources such as high expressivity yielding unitary 2-designs [5] and volume-law entanglement [6], unified in a Lie-algebraic framework [10, 11]. Trainability is further challenged by spurious local minima [12–14] and noise effects [15–19].

Entanglement's role is paradoxical: vital for quantum advantage, yet excessive amounts cause issues, such as inefficient "CQ–universality" (classical-input/quantum-output) in measurement-based quantum computing [20, 21] and barren plateaus in VQAs that hinder gradient-based and gradient-free optimizers through equivalent cost concentra-

tion [22, 23]. Mitigation strategies target circuit and cost function structure constraints [24–31], altering the training protocol [32–34], and employing specialized initializations [29, 35, 36]. However, it is worth noting that despite these efforts, the absence of barren plateaus alone does not guarantee a quantum advantage [37]. Recent analyses highlight that successful training may still require increasingly precise initializations [38] and that even trainable regions might be classically surrogatable with only polynomial overhead (after potentially identifying necessary basis with quantum computers) [39].

We address these issues using *many-body localization* (MBL), a phenomenon in disordered quantum systems featuring a thermal-to-localized transition with increasing disorder [40–44]. Thermal phases show volume-law entanglement entropy [45], while MBL phases exhibit area-law scaling, preserving localization. MBL's local integrals of motion and decoherence resilience [43] have spurred quantum computing applications, including annealing acceleration [46], VQE probing [47], analog expressibility [48], Floquet Trotterization [49, 50], and experimental integral extraction [51].

Recent works have also linked MBL to improved VQA trainability, in both digital hardware-efficient circuits [52] and analog VQAs where phases of matter are closely tied to the flatness of the loss landscape [53]. In contrast, our work uses a distinct circuit architecture and trial-state construction, provides a t-design-based analytical explanation, and includes an experimental demonstration on a 127-qubit processor.

Inspired by Floquet MBL dynamics [54–56], we develop a Floquet-initialized, hardware-efficient, universal variational circuit exhibiting an MBL–thermalization transition [54, 55]. By initializing the circuit within the MBL phase—characterized by area-law entanglement and robust gradients—our protocol systematically avoids barren plateaus. The optimization begins from a low-complexity trial state and, while expressibility is unrestricted during training, our data suggest that for the Hamiltonians and system sizes studied, optimization trajectories remain in trainable regions, far from the 2-design limit that causes plateaus.

We validate our proposal with tools linking t-designs to MBL: a relation via inverse participation ratio (Theorem 1) and a new low-weight stabilizer Rényi entropy $M_{t,k}$ correlating with higher-order ($2t$-) designs (Theorem 2). These results provide insight into circuit randomness, and under plausible assumptions, provide evidence for barren-plateau absence in MBL (Observation 1, Theorem 3). On the experimental side, we implement our protocol on the 127-qubit `ibm_brisbane` processor, successfully demonstrating gradient restoration for a kicked Heisenberg model of up to 31 qubits.

The paper is organized as follows: Section 2 details Floquet-initialized circuits; Section 3 examines the MBL–thermalization transition; Section 4 discusses trainability and Aubry-André applications; Section 5 presents experimental results; Section 6 summarizes findings and future directions. In Appendices, we provide proofs of universality, theorems, and additional analyses.

2 Methods

Our approach employs an n-qubit hardware-efficient layered ansatz. As depicted in Fig. 1(a), each of the D layers consists of a fixed sequence of blocks containing single-qubit and two-qubit Pauli rotations. This ansatz is universal, capable of approximating any unitary transformation with sufficient depth (see Appendix A for a constructive proof).

The variational optimization begins from a low-complexity, classically obtained trial state $|\psi_t\rangle$ (e.g., a Hartree–Fock Slater determinant or a compact matrix-product state [57–59]). The construction of $|\psi_t\rangle$ aims to capture essential features of the target ground state's entanglement structure. Let $\rho_t := |\psi_t\rangle\langle\psi_t|$. We then apply a low-depth quantum channel $\mathcal{E}_t$ that maps this trial state to a simple reference state in the computational basis, $\rho_c := \mathcal{E}_t(\rho_t) = |\varphi_c\rangle\langle\varphi_c|$ (e.g., $|\uparrow\rangle^{\otimes n}$). The main variational circuit $\hat{U}(\boldsymbol{\vartheta})$ is then applied to $|\varphi_c\rangle$, and a decoding channel $\mathcal{E}_t^{-1}$ reverses the encoding defined by $\mathcal{E}_t$ on the relevant family of states explored. When viewed in the logical frame defined by $\mathcal{E}_t$, the evolution is effectively conjugated by $\mathcal{E}_t$ and $\mathcal{E}_t^{-1}$. This ensures that the evolution remains quasi-local with respect to the degrees of freedom already localized in $|\psi_t\rangle$, thereby preserving MBL-like properties at initialization. Ultimately, our method should be viewed as the

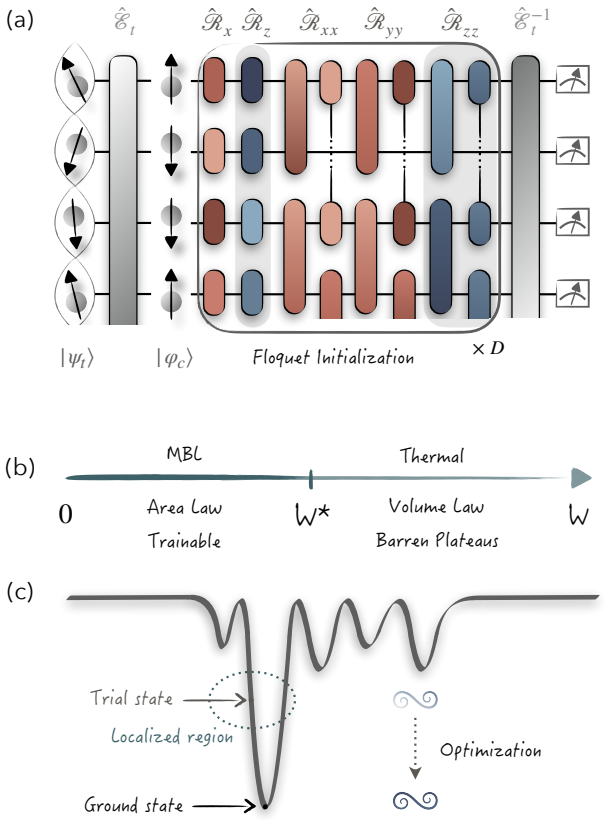


Figure 1: Schematic representation of the Floquet-initialized variational quantum circuit, the localization-thermalization phase transition, and the optimization landscape. **(a)** Diagram of a variational quantum circuit. The illustration includes four qubits as a segment of a larger circuit, resulting in some 2-qubit gates acting on adjacent pairs $Q_i - Q_j$ appearing truncated. The circuit begins with a low-complexity trial state. Steady rotation angles within $\hat{\mathcal{R}}_z$ and $\hat{\mathcal{R}}_{zz}$ are initialized randomly within $[-\pi, \pi)$, while the kick rotation angles in $\hat{\mathcal{R}}_x$, $\hat{\mathcal{R}}_{xx}$, and $\hat{\mathcal{R}}_{yy}$ are initialized within $[-W, W]$. **(b)** Transition of the variational quantum circuit between the many-body localized (MBL) phase and the thermal phase as a function of the kick strength W. Below a critical threshold $W^\star$, the circuit remains in the MBL phase, characterized by output state entanglement entropy adhering to the area law and trainable circuit parameters. Above $W^\star$, the circuit enters the thermal phase, where the output state's entanglement entropy follows the volume law, rendering the circuit parameters untrainable. **(c)** Depiction of the optimization landscape for an MBL-initialized circuit. The initial output state is localized to a trial state, ideally positioned in the same "valley" as the ground state, facilitating effective optimization.

second step in an optimization scheme in which the first step is the best possible classical computation.

The main variational circuit contains parameters that implement the Floquet initialization:

$$\hat{U}(\boldsymbol{\vartheta}) = \prod_{\ell=1}^{D} \Big(\prod_{\substack{\alpha\in \\ \{x,y,z\}}} \hat{\mathcal{R}}_{\alpha\alpha}(\boldsymbol{\vartheta}_{\alpha\alpha}^{(\ell)}) \Big) \Big(\prod_{\alpha\in\{x,z\}} \hat{\mathcal{R}}_{\alpha}(\boldsymbol{\vartheta}_{\alpha}^{(\ell)}) \Big). \tag{1}$$

Here, D denotes the circuit depth, measured by the number of layers. For Pauli index $\alpha \in \{x, y, z\}$, we define:

$$\hat{\mathcal{R}}_{\alpha}(\boldsymbol{\vartheta}_{\alpha}^{(\ell)}) = \prod_{j=1}^{n} \exp\Big(-i\frac{\vartheta_{\alpha}^{(\ell j)}}{2}\hat{\sigma}_j^{\alpha}\Big),$$

$$\hat{\mathcal{R}}_{\alpha\alpha}(\boldsymbol{\vartheta}_{\alpha\alpha}^{(\ell)}) = \prod_{(j,k)\in \mathrm{edges}(G)} \exp\Big(-i\frac{\vartheta_{\alpha\alpha}^{(\ell jk)}}{2}\hat{\sigma}_j^{\alpha}\hat{\sigma}_k^{\alpha}\Big), \tag{2}$$

where $\boldsymbol{\vartheta}_{\alpha}^{(\ell)}$ represents the rotation angles for single-qubit α-Pauli rotations in the ℓ-th layer, and $\boldsymbol{\vartheta}_{\alpha\alpha}^{(\ell)}$ denotes those for two-qubit $\alpha\alpha$-Pauli rotations in the same layer. The graph G specifies the qubit connectivity for two-qubit gates.

The Floquet initialization begins by uniformly sampling first-layer *steady parameters* $\vartheta_z^{(1j)}$ and $\vartheta_{zz}^{(1jk)}$ from $[-\pi, \pi)$, and *kick parameters* $\vartheta_x^{(1j)}$, $\vartheta_{xx}^{(1jk)}$, $\vartheta_{yy}^{(1jk)}$ from $[-W, W]$, where W is the kick strength. These are replicated across all layers $\ell = 1, 2, \ldots, D$:

$$\boldsymbol{\vartheta}_{\alpha}^{(\ell)} = \boldsymbol{\vartheta}_{\alpha}^{(1)}, \quad \boldsymbol{\vartheta}_{\alpha\alpha}^{(\ell)} = \boldsymbol{\vartheta}_{\alpha\alpha}^{(1)}, \quad \forall\, \ell \in \{1, \ldots, D\}. \tag{3}$$

yielding an initial parameter instance $\boldsymbol{\vartheta}_{\mathrm{init}}$ drawn from the periodic ensemble $\Theta_{\mathrm{prd}}(W)$.

This Floquet initialization corresponds to a digital simulation of a periodically driven many-body system. At initialization (when $\boldsymbol{\vartheta} \in \Theta_{\mathrm{prd}}(W)$), all layers share identical parameters, so the single-layer unitary $\hat{U}_1$ acts as the Floquet operator and the initialized circuit is $\hat{U}_1^D$. Since gates within each block commute [Eq. (2)], each block is the exact exponential of a (few-body) Hamiltonian term. Defining, for $\alpha \in \{x, z\}$,

$$\hat{H}_{\alpha} = \frac{1}{2}\sum_j \vartheta_{\alpha}^{(1j)}\hat{\sigma}_j^{\alpha}, \tag{4}$$

and for $\alpha \in \{x, y, z\}$,

$$\hat{H}_{\alpha\alpha} = \frac{1}{2}\sum_{(j,k)\in \mathrm{edges}(G)} \vartheta_{\alpha\alpha}^{(1jk)}\hat{\sigma}_j^{\alpha}\hat{\sigma}_k^{\alpha}, \tag{5}$$

the Floquet operator (up to the chosen block ordering within a layer) can be written as

$$\hat{U}_1 = e^{-i\hat{H}_{zz}} e^{-i\hat{H}_{yy}} e^{-i\hat{H}_{xx}} e^{-i\hat{H}_z} e^{-i\hat{H}_x}. \tag{6}$$

One convenient representation is a piecewise-constant drive over one period T, e.g. $\hat{H}(t) = \hat{H}_x$ for $t \in [0,1)$, $\hat{H}_z$ for $t \in [1,2)$, $\hat{H}_{xx}$ for $t \in [2,3)$, $\hat{H}_{yy}$ for $t \in [3,4)$, and $\hat{H}_{zz}$ for $t \in [4,5)$ (and periodic), which yields $\hat{U}_1 = \mathcal{T} e^{-i\int_0^T dt \hat{H}(t)}$, with $\mathcal{T}$ denoting time ordering. The steady angles are sampled uniformly from $[-\pi, \pi)$, which provides strong quenched disorder; Floquet-MBL is known to persist in such disordered interacting drives for sufficiently weak driving [43, 54–56], and has been demonstrated numerically in related disordered Floquet spin-chain models [60]. In our parametrization, W controls the typical magnitude of the kick generators: small W yields localized (Floquet-MBL) dynamics dominated by the steady disorder, while large W induces thermalization.

A subtlety specific to periodically driven systems is the distinction between genuine Floquet-MBL (no heating even at asymptotically long times) and Floquet prethermal regimes, where heating is parametrically slow and the dynamics is well captured by an effective quasi-conserved Hamiltonian over exponentially long times before eventual heating sets in [61–63]. In the near-term variational setting considered here, however, this distinction is largely immaterial: our circuits have finite depth and run on noisy hardware with finite coherence, so what matters is simply the existence of a long-lived non-ergodic window over the explored depths, during which entanglement remains low and the circuit stays far from unitary-design behavior. Accordingly, we use the term "MBL phase" operationally to denote this trainable non-ergodic regime.

This Floquet initialization is fundamentally distinct from close-to-identity schemes [29, 36, 64], where layer parameters are typically drawn independently near the identity. Here, strict layer replication ($\hat{U}_\ell = \hat{U}_1$ at initialization) is essential: it realizes stroboscopic evolution under a fixed disordered Floquet drive, as required in Floquet-MBL constructions.

For each layer unitary $\hat{U}_\ell$ we denote its induced channel by $\mathcal{U}_\ell(\rho) := \hat{U}_\ell \rho \hat{U}_\ell^\dagger$. It is convenient to describe the dynamics in the logical frame defined by the encoding channel $\mathcal{E}_t$, in which each physical layer $\mathcal{U}_\ell$ appears conjugated as $\mathcal{E}_t^{-1} \circ \mathcal{U}_\ell \circ \mathcal{E}_t$. In this frame, the initialized circuit acts as

$$\begin{aligned}\rho(\boldsymbol{\vartheta}_{\text{init}}) &= (\mathcal{E}_t^{-1} \circ \mathcal{U}_D \circ \mathcal{E}_t) \cdots (\mathcal{E}_t^{-1} \circ \mathcal{U}_1 \circ \mathcal{E}_t)(\rho_t) \\ &= (\mathcal{E}_t^{-1} \circ \mathcal{U}_1 \circ \mathcal{E}_t)^{\circ D}(\rho_t) \\ &= (\mathcal{E}_t^{-1} \circ \mathcal{U}_1^{\circ D} \circ \mathcal{E}_t)(\rho_t)\end{aligned} \tag{7}$$

Each "effective" layer $(\mathcal{E}_t^{-1} \circ \mathcal{U}_\ell \circ \mathcal{E}_t)$ acts in the logical basis where $|\psi_t\rangle$ is a simple product state; hence its generators are quasi-local in the $\mathcal{E}_t$-defined logical basis (i.e., with respect to the degrees of freedom captured by the trial state). In the sense of circuit expressibility defined in Refs. [7, 65], Floquet replication greatly restricts the effective exploration of parameter space compared to fully random layer-wise parametrizations, leading to a slower increase in expressibility than in fully random circuits and keeping it, for the system sizes studied, below the unitary-2-design threshold.

During optimization, rotation angles in different layers are updated independently to minimize the output energy. With sufficient depth and suitable parameters, the variational quantum circuit can in principle prepare the exact ground state of the target Hamiltonian. While the output state is not confined to the vicinity of $|\psi_t\rangle$ during optimization—indicating release from strict MBL constraints—numerical evidence in Sec. 4 suggests that MBL-based initialization keeps the optimization trajectories far from the Haar regime for the system sizes and models studied, and we did not observe barren-plateau behavior along these trajectories. A more systematic validation across broader settings and larger system sizes is left to future work. In principle, $\mathcal{E}_t$ could be a general (possibly non-unitary) encoding channel. In this work, for implementability we take $\mathcal{E}_t(\rho) = U_t \rho U_t^\dagger$ with a shallow unitary U_t, so that $\mathcal{E}_t^{-1}(\rho) = U_t^\dagger \rho U_t$.

3 MBL–Thermalization Transition

Many-body localization (MBL) arises in disordered quantum systems with interacting constituents, where disorder can trigger a transition from ergodic to non-ergodic behavior [40–43]. Consequently the system fails to thermalize and retains memory of its initial conditions. In this section, we analyze the MBL–thermalization phase transition in our setup using three diagnostics: inverse participation ratio (IPR), entangle-

ment entropy, and a low-weight stabilizer Rényi entropy (SRE).

We briefly recall the concept of quantum t-designs, critical for analyzing random quantum states and channels [66–68]. An ensemble of parameterized unitary operations $\hat{U}(\boldsymbol{\vartheta})$, with $\boldsymbol{\vartheta}$ uniformly sampled from the parameter space Θ, forms a t-design if and only if it satisfies

$$\int_{\Theta}(\hat{U}(\boldsymbol{\vartheta})\otimes\hat{U}(\boldsymbol{\vartheta})^{\dagger})^{\otimes t}d\boldsymbol{\vartheta}=\int_{\mathrm{U}(2^n)}(\hat{U}\otimes\hat{U}^{\dagger})^{\otimes t}d\mu_{\mathrm{H}}(\hat{U}), \tag{8}$$

where $\mathrm{U}(2^n)$ denotes the unitary group and $d\mu_{\mathrm{H}}(\hat{U})$ is the Haar measure, i.e. the unique left- and right-invariant probability measure on $\mathrm{U}(2^n)$ that serves as the "uniform" distribution over all unitaries [69, 70].

Within the context of variational quantum optimization, if the circuit ensemble forms a unitary 2-design then cost gradients concentrate exponentially in the system size, independently of the cost locality [5, 24]. While real-valued, time-reversal-symmetric circuits are expected to thermalize to the circular orthogonal ensemble (COE) [71, 72], our hardware-efficient ansatz employs non-commuting generators that span $\mathfrak{su}(2^n)$. This structure generally breaks time-reversal symmetry, meaning the unitary cannot be represented solely by a real matrix. Consequently the thermal phase is governed by the circular unitary ensemble (CUE). A level-statistics check (Appendix B) shows the disorder-averaged adjacent-gap ratio approaching the CUE benchmark $\langle r\rangle \simeq 0.603$ (as opposed to $\simeq 0.536$ for COE and $\simeq 0.386$ for Poisson), justifying the use of Haar–$\mathrm{U}(2^n)$ moments in our t-design benchmarks.

Inverse Participation Ratio– The inverse participation ratio (IPR) is a valuable metric for characterizing the localization properties of quantum states. For an n-qubit state $|\psi\rangle$, the t-th-order IPR with respect to the basis states $\{|\beta_j\rangle\}$ is defined as

$$\mathrm{IPR}_t(|\psi\rangle)=\sum_j|\langle\beta_j|\psi\rangle|^{2t}. \tag{9}$$

A higher IPR_t value indicates a more localized state, while a lower value indicates greater delocalization. As t increases, the IPR becomes increasingly sensitive to localization properties. In MBL studies, IPR_2 is commonly used to differentiate between localized and delocalized eigenstates [73, 74]. Here, we select basis states $\{|\beta_j\rangle = \hat{U}_t^{\dagger}|j\rangle\}$ with $\{|j\rangle\}_{j=1,2,\ldots,2^n}$ representing the computational basis. The trial state $|\psi_t\rangle$ belongs to $\{|\beta_j\rangle\}$. The IPR_t measures how well the output state is localized to the trial state, noting that IPR's definition is basis-dependent.

There is a profound link between the inverse participation ratio and the t-design characteristic:

Theorem 1 *Assume that $\{\hat{U}(\boldsymbol{\vartheta})\}$, with $\boldsymbol{\vartheta}$ uniformly sampled from Θ, forms a unitary t-design. For any arbitrary n-qubit input state $|\psi_{in}\rangle$, the expected value of the inverse participation ratio of the output state $|\psi(\boldsymbol{\vartheta})\rangle = \hat{U}(\boldsymbol{\vartheta})|\psi_{in}\rangle$ with respect to some basis states $\{|\beta_j\rangle\}$ satisfies*

$$\int_{\Theta}IPR_t(|\psi(\boldsymbol{\vartheta})\rangle)d\boldsymbol{\vartheta}=\frac{2^n!\,t!}{(t+2^n-1)!}. \tag{10}$$

For $t=2$, specifically:

$$\int_{\Theta}IPR_2(|\psi(\boldsymbol{\vartheta})\rangle)d\boldsymbol{\vartheta}=\frac{2}{2^n+1}. \tag{11}$$

A proof is available in Appendix C.

This result indicates that the inverse participation ratio not only quantifies localization but also provides a diagnostic for whether an ensemble of unitaries violates unitary t-design behavior. However, unlike the frame potential defined in Refs. [66, 75], IPR_t is not suitable for quantifying the deviation of $\{|\psi(\boldsymbol{\vartheta})\rangle\}$ from t-designs with $t\geq 2$, as the basis states $\{|\beta_j\rangle\}$ do not form a state 2-design. Instead, when $t\geq 2$, the dimension of the subspace spanned by the t-fold basis states is considerably smaller than the dimension of the t-fold symmetric subspace $\vee^t\mathbb{C}^{2^n}$ [76]:

$$\begin{aligned}\dim(\mathrm{Span}\{|j\rangle^{\otimes t}\}) &= 2^n\\ &\ll \dim(\vee^t\mathbb{C}^{2^n})\\ &= \binom{t+2^n-1}{t}.\end{aligned} \tag{12}$$

Despite these dimensional differences, we confirm that in the thermal phase, the output state ensemble qualifies as a state 2-design. This confirmation comes from our direct calculations of frame potentials, detailed in Appendix D. Additionally, we explore the expressibility of the Floquet initialization for both the MBL and thermal phases in the same appendix, providing insights into the dynamic behaviors of these phases.

Entanglement Entropy– A pivotal characteristic of MBL is the behavior of the von Neumann entanglement entropy (S_L) of a subsystem L:

$$S_L = -\operatorname{Tr}(\rho_L \log \rho_L) \tag{13}$$

where ρ_L is the reduced density matrix for subsystem L. In thermalized systems, S_L adheres to a volume law scaling, proportional to subsystem size: $S_L \sim |L|^d$, where d denotes the spatial dimension of the system. In contrast, MBL systems exhibit an area law scaling, in which S_L increases proportionally to the boundary of the subsystem L: $S_L \sim |L|^{d-1}$ [45]. For one-dimensional systems, where $d = 1$, S_L essentially remains constant. The transition from volume law to area law scaling is a defining characteristic of MBL systems and has been extensively studied through numerical simulations [74, 77].

Low-Weight Stabilizer Rényi Entropy– The final metric we employ is a restricted version of the stabilizer Rényi entropy, as defined in Ref. [78], which aims to quantify the magic resource (non-stabilizerness) of a quantum state. This metric provides valuable insights into quantum many-body systems, enhancing our understanding of complex patterns in ground-state wave functions [79] and the dynamics of quantum quenches [80]. Unlike the original definition, which encompasses all Pauli terms and is thus challenging to estimate in practical scenarios, our approach focuses solely on low-weight Pauli terms. We define the low-weight stabilizer Rényi entropy as follows:

Definition 1 (low-weight SRE) *Given an n-qubit state $|\psi\rangle$, we define its low-weight stabilizer Rényi entropy of order t and locality k as*

$$M_{t,k}(|\psi\rangle) = (1-t)^{-1} \log \sum_{\hat{P}\in\mathcal{P}_{n,k}} \frac{|\langle\psi|\hat{P}|\psi\rangle|^{2t}}{\operatorname{card}(\mathcal{P}_{n,k})}, \tag{14}$$

where $\mathcal{P}_{n,k}$ is the set of n-qubit Pauli strings (including the identity) with phase $+1$ and Pauli weight $w(\hat{P}) \le k$.

This metric characterizes the extent to which a quantum state $|\psi\rangle$ can be stabilized by some low-weight Pauli tensor products, a concept particularly relevant in quantum error correction contexts [81].

In the Floquet-MBL regime ($W < W^\star$), the dynamics admit an extensive set of quasi-local integrals of motion (the ℓ-bits), $\{\hat{\tau}_j^z\}_{j=1}^n$. Deep in the localized phase, the memory of the initial computational basis state is preserved, implying that each $\hat{\tau}_j^z$ maintains an $\mathcal{O}(1)$ overlap with the local Pauli operator $\hat{\sigma}_j^z$. Consequently, there exist constants $\beta(W) > 0$ and a subset $\mathcal{Z}_{n,k} \subseteq \mathcal{P}_{n,k}$ consisting of Z-strings with $|\mathcal{Z}_{n,k}| = \Theta(n^k)$ such that for all $\hat{P}_S \in \mathcal{Z}_{n,k}$ one has $|\langle\psi|\hat{P}_S|\psi\rangle| \ge \beta(W)$. Since the total cardinality of the Pauli set scales as $|\mathcal{P}_{n,k}| = \sum_{w=0}^k 3^w \binom{n}{w} = \Theta(3^k n^k)$, these structured correlations constitute a constant fraction $\Theta(3^{-k})$ of $\mathcal{P}_{n,k}$. Therefore, the average overlap scales as

$$\begin{aligned}\frac{1}{\operatorname{card}(\mathcal{P}_{n,k})} \sum_{\hat{P}\in\mathcal{P}_{n,k}} |\langle\psi|\hat{P}|\psi\rangle|^{2t} &\ge \Theta(3^{-k})\,\beta(W)^{2t} \\ &= \Theta(1),\end{aligned} \tag{15}$$

which implies that $M_{t,k}$ remains $\mathcal{O}(1)$ for all n (at fixed t, k) throughout the MBL phase ($W < W^\star$).

By contrast, in the thermal phase ($W > W^\star$), the eigenstate thermalization hypothesis suggests $|\langle\psi|\hat{P}|\psi\rangle| = \mathcal{O}(2^{-n/2})$ for any fixed-weight $\hat{P}$. Because $M_{t,k}$ is a moment-generating functional of the overlaps in Eq. (14), the bound in Eq. (15) keeps $M_{t,k}$ of order unity in the MBL phase, whereas in the thermal phase the overlaps become exponentially small and $M_{t,k}$ approaches its Haar benchmark. This suggests that the difference between $M_{t,k}$ and its Haar benchmark serves as a potential order parameter for the MBL–thermalization transition.

Beyond its physical relevance, $M_{t,k}$ also quantifies how close the output-state ensemble is to forming higher-order designs, as it depends on the $(2t)$-th moments of the distribution:

Theorem 2 *Assume that $\{\hat{U}(\boldsymbol{\vartheta})\}$, with $\boldsymbol{\vartheta}$ uniformly sampled from Θ, forms a unitary $2t$-design. Then any arbitrary n-qubit input state $|\psi_{in}\rangle$ transformed by these operations satisfies:*

$$\begin{aligned}&\int_\Theta \frac{1}{\operatorname{card}(\mathcal{P}_{n,k})} \sum_{\hat{P}\in\mathcal{P}_{n,k}} \langle\psi(\boldsymbol{\vartheta})|\hat{P}|\psi(\boldsymbol{\vartheta})\rangle^{2t} d\boldsymbol{\vartheta} \\ &= \frac{\binom{2^n+2t-1}{2t} - \binom{2^{n-1}+t-1}{t}}{\operatorname{card}(\mathcal{P}_{n,k})\binom{2^n+2t-1}{2t}} + \frac{\binom{2^{n-1}+t-1}{t}}{\binom{2^n+2t-1}{2t}}.\end{aligned} \tag{16}$$

Let this value be denoted by $T_{t,k}$. By Jensen's inequality, the expected low-weight stabilizer Rényi

entropy of order t and locality k of $|\psi(\boldsymbol{\vartheta})\rangle$ satisfies:

$$\int_{\Theta} M_{t,k}(|\psi(\boldsymbol{\vartheta})\rangle) d\boldsymbol{\vartheta} \geq \frac{\log(T_{t,k})}{1-t}. \tag{17}$$

Thus, computing $M_{t,k}$ provides a convenient witness against $2t$-design behavior from low-weight moments. We denote the right-hand side of Inequality (17) as $\widetilde{M}_{t,k}^{(\mathrm{Haar})}$. Specifically, $M_{2,2}$ probes fourth moments (hence 4-design signatures). A significant deviation from the Haar benchmark indicates that the output ensemble is far from Haar-random at the level of fourth moments; in our setting this correlates with, and provides evidence for, staying away from the unitary-2-design regime relevant to barren plateaus. The proof for Theorem 2 is provided in Appendix E.

Characterizing MBL and Thermalization– Utilizing the inverse participation ratio, entanglement entropy, and the low-weight stabilizer Rényi entropy as metrics, we investigate the MBL–thermalization phase transition in a layered "square circuit" whose layer depth equals the system size, $D = n$. With n qubits, each layer contains $\Theta(n)$ one- and two-qubit rotations, so the total number of elementary gates is $\Theta(nD) = \Theta(n^2)$. Such circuits are known to exhibit barren plateaus when all parameters are chosen independently at random [24].

Unless stated otherwise, the trial state is taken to be a product state

$$|\psi_t\rangle = \bigotimes_{j=1}^{n} U_j^{(\mathrm{Haar})} |\uparrow\rangle_j, \tag{18}$$

where each $U_j^{(\mathrm{Haar})}$ represents a single-qubit Haar-random unitary operation applied to qubit Q_j. A shallow unitary $\hat{U}_t$ then maps $|\psi_t\rangle$ to the computational basis state of highest overlap.

We study two graphs:

- A 1D ring, in which each qubit is coupled only to its nearest neighbors.
- A *circulant graph* $\mathrm{Ci}_n(1,2)$, in which each qubit Q_j is coupled to qubits $Q_{j\pm1}$ and $Q_{j\pm2}$ (mod n), i.e. edges of length 1 *and* 2 around the ring.

The results for average IPR_2, half-chain entanglement entropy and its fluctuations, and $M_{2,2}$ are depicted in Fig. 2 with each point averaged over at least 200 samples.

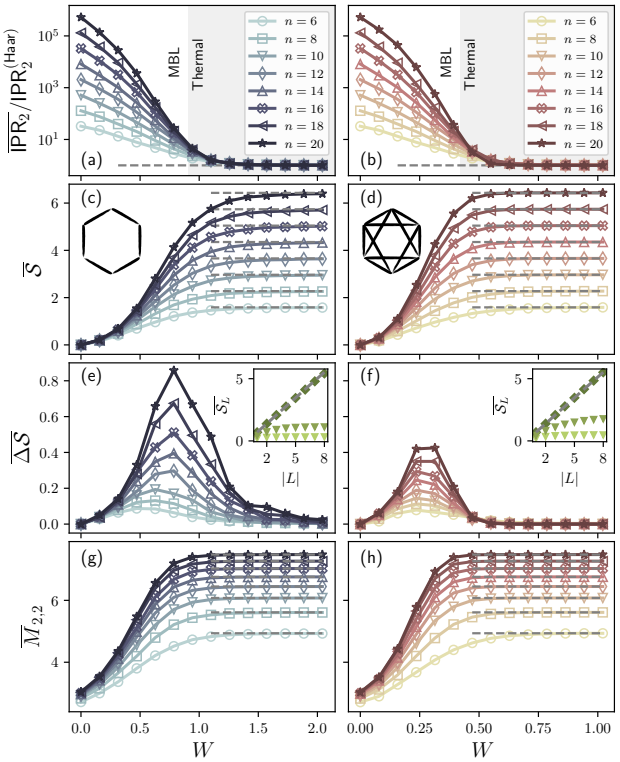


Figure 2: Characterization of the MBL–thermalization transition. Panels (a, c, e, g) represent results for the 1D ring topology, and panels (b, d, f, h) represent results for the $\mathrm{Ci}_n(1,2)$ topology. **(a, b)** Ratios of the inverse participation ratio, IPR_2 [Eq. (11)], to the Haar-random inverse participation ratio, $\mathrm{IPR}_2^{(\mathrm{Haar})}$ [Eq. (21)], as a function of kick strength W. The grey dashed lines correspond to 1. **(c, d)** Half-chain entanglement entropy versus kick strength W. The grey dashed lines correspond to $S^{(\mathrm{Page})}$ [Eq. (22)]. Insets: Demonstration of the topologies of a 6-qubit ring and a $\mathrm{Ci}_6(1,2)$ graph. **(e, f)** Entanglement entropy fluctuations versus kick strength W. Insets: Entanglement entropy of a local region L versus the size of L for both MBL ($W = 1/5, 2/5$ for the 1D ring topology and $W = 1/10, 1/5$ for the $\mathrm{Ci}_n(1,2)$ topology) and thermal ($W = 7/5$ for 1D ring and $W = 7/10$ for $\mathrm{Ci}_n(1,2)$) phases in a 20-spin chain. Darker green markers indicate circuits with higher W. The grey dashed lines correspond to $S^{(\mathrm{Page})}$. **(g, h)** The low-weight stabilizer Rényi entropy of order 2 and locality 2 [Eq. (14)] versus kick strength W. The grey dashed lines correspond to the lower bound $\widetilde{M}_{2,2}^{(\mathrm{Haar})}$ [Eq. (24)].

To systematically estimate the critical kick strength $W^\star$ we use an operational, finite-size criterion. For each system size n we scan W on a fine grid, record three diagnostics (i) $\log_{10}\overline{\mathrm{IPR}_2}$, (ii) half-chain entropy $\overline{S}(n/2, n)$, (iii) low-weight stabilizer Rényi entropy $\overline{M}_{2,2}$. Spline fits to these

observables yield the transition points as the positions of maximal susceptibility

$$W^\star_{\mathcal{X}}(n) = \arg\max_W |\partial^2_W \mathcal{X}(W)|. \tag{19}$$

for $\mathcal{X} \in \{\log \mathrm{IPR}_2, S, M_{2,2}\}$. We quote the crossover as the average over the three observables and all n considered,

$$W^\star = \frac{1}{3}(\overline{W^\star}_{\log \mathrm{IPR}_2} + \overline{W^\star}_S + \overline{W^\star}_{M_{2,2}}), \tag{20}$$

giving $W^\star \approx 0.90$ for the 1D ring and $W^\star \approx 0.42$ for $\mathrm{Ci}_n(1,2)$; the spread among the three estimates is around 0.1.

For both graph types, when the kick strength is below a certain threshold $W^\star$, the output state remains localized to the trial state:

$$\overline{\mathrm{IPR}}_2 \gg \mathrm{IPR}_2^{(\mathrm{Haar})} = \frac{2}{2^n+1}; \tag{21}$$

the average half-chain entanglement entropy, $\overline{S}(\frac{n}{2}, n)$, is significantly lower than the Page value for a random pure state, $S^{(\mathrm{Page})}(\frac{n}{2}, n)$ [82, 83]:

$$\begin{aligned}\overline{S}\left(\frac{n}{2}, n\right) &\ll S^{(\mathrm{Page})}\left(\frac{n}{2}, n\right) \\ &= \sum_{j=2^{n/2}+1}^{2^n} \frac{1}{j} - \frac{2^{n/2}-1}{2\cdot 2^{n/2}};\end{aligned} \tag{22}$$

the entanglement entropy fluctuation, quantified by the sample variance $\overline{\Delta\mathcal{S}} := \mathrm{Var}[S(n/2, n)]$, is substantial; and the output state can be stabilized by some low-weight Pauli stabilizers to a certain extent

$$\overline{M}_{2,2} \ll M_{2,2}^{(\mathrm{Haar})} = \log(\mathrm{card}(\mathcal{P}_{n,2})) - \mathcal{O}(2^{-n}). \tag{23}$$

A convenient analytic lower bound on $M_{2,2}^{(\mathrm{Haar})}$ obtained from the exact moment formula with $2t = 4$ is

$$\begin{aligned}\widetilde{M}_{2,2}^{(\mathrm{Haar})} = -\log\Bigg(&\frac{1}{\mathrm{card}\,\mathcal{P}_{n,2}} \\ &+ \left(1 - \frac{1}{\mathrm{card}\,\mathcal{P}_{n,2}}\right)\frac{\binom{2^{n-1}+1}{2}}{\binom{2^n+3}{4}}\Bigg).\end{aligned} \tag{24}$$

When $W > W^\star$, IPR_2 approaches $2/(2^n+1)$, $\overline{S}$ approaches $S^{(\mathrm{Page})}$, $\overline{\Delta\mathcal{S}}$ collapses to zero, and $\overline{M}_{2,2}$ gets close to

$$\log(\mathrm{card}(\mathcal{P}_{n,2})) = \log\left(\frac{9n^2}{2} - \frac{3n}{2} + 1\right). \tag{25}$$

Insets for a 20-qubit system illustrate that the entanglement entropy in the MBL phase (with $W = 1/5, 2/5$ for the 1D ring and $W = 1/10, 2/10$ for $\mathrm{Ci}_n(1,2)$) follows the area law, while entanglement entropy in the thermal phase adheres to the volume law. It is conjectured (and has been proven for 1D systems) that the entanglement of the ground states of gapped spin systems obeys the area law [45, 84]. When preparing these states with variational quantum optimization, it is reasonable to initialize the variational quantum circuits in the MBL phase to maintain consistency in entanglement entropy and, preferably, entanglement structure. The optimal choice of the kick strength W depends on the hardware topology, circuit depth, and the entanglement properties of the ground state of the target Hamiltonian. Though these numerical results primarily pertain to square circuits, local information remains well-preserved even in deeper circuits. Detailed illustrations are available in Appendix F.

4 Variational Optimization

This section examines the performance of the VQE in preparing the ground state of the Aubry-André model across different phases [85]. The Aubry–André model, extensively studied in condensed matter physics, characterizes a one-dimensional system of spinless fermions with nearest-neighbor hopping and a quasiperiodic on-site potential. The system's phase transitions are governed by the ratio of the quasiperiodic potential strength V to the hopping amplitude J. Its Hamiltonian is:

$$\begin{aligned}\hat{\mathcal{H}}_{\mathrm{AA}}^{(\mathrm{fm})} = &-J\sum_j(\hat{c}_j^\dagger\hat{c}_{j+1} + \hat{c}_{j+1}^\dagger\hat{c}_j) + \Gamma\sum_j \hat{n}_j\hat{n}_{j+1} \\ &+ V\sum_j \cos(2\pi\alpha j + \phi)\hat{n}_j,\end{aligned} \tag{26}$$

where $\hat{c}_j^\dagger$, $\hat{n}_j$, and ϕ denote the usual fermionic creation, number operators, and phase offset, respectively.

In the non-interacting limit ($\Gamma = 0$), the model undergoes a transition from Anderson localization to an extended phase at a critical point determined by the ratio $|V|/|J|$, with localization occurring when $|V| > 2|J|$ and delocalization when $|V| < 2|J|$. Upon introducing nearest-neighbor repulsive interactions ($\Gamma > 0$), the system exhibits transitions between MBL and er-

godic phases [86]. We emphasize that "MBL initialization" and "thermal initialization" refer exclusively to initial parameter ensembles of the variational circuit. Our protocol employs distinct trial states for different phases of the model, yet these initializations neither constrain the many-body phase of the target Hamiltonian nor restrict the optimization trajectory, as circuit parameters evolve freely after the initial optimization step.

Utilizing the Jordan-Wigner transformation [87], the qubit form of the Aubry-André model is derived as:

$$\hat{\mathcal{H}}_{\mathrm{AA}} = -\frac{J}{2}\sum_j (\hat{\sigma}_j^x\hat{\sigma}_{j+1}^x + \hat{\sigma}_j^y\hat{\sigma}_{j+1}^y) + \frac{\Gamma}{4}\sum_j \hat{\sigma}_j^z\hat{\sigma}_{j+1}^z - \frac{V}{2}\sum_j [\cos(2\pi\alpha j + \phi) + \Gamma/V]\hat{\sigma}_j^z. \tag{27}$$

Before discussing variational optimization, we recall the notion of a *weak barren plateau* introduced in Ref.[33], the avoidance of which is sufficient to prevent barren plateaus. We also explain why bounding the von Neumann entropy is sufficient to exclude their occurrence.

An ensemble of states $|\psi(\boldsymbol{\vartheta})\rangle$ is said to exhibit a weak barren plateau if for every connected region L of at most k qubits the second Rényi entropy $S_L^{(2)} := -\log\left(\mathrm{Tr}(\rho_L^2)\right)$ satisfies

$$S_L^{(2)} \geq (1-\delta)S^{(\mathrm{Page})}(k,n), \quad 0<\delta<1, \tag{28}$$

where $S^{(\mathrm{Page})}(k,n)$ is the Page entropy of a k-qubit subsystem of an n-qubit Haar-random pure state. Condition (28) implies that the variance of any k-local cost function scales as $\mathcal{O}(2^{-n})$, resulting in gradients that concentrate around zero [33].

Since Rényi entropies decrease monotonically with their order, we always have $S_L^{(2)} \leq S_L$. Therefore, an upper bound of the form

$$S_L < \xi S^{(\mathrm{Page})}(k,n), \quad \xi < 1-\delta, \tag{29}$$

precludes condition (28), thus sufficing to rule out the occurrence of randomness-induced barren plateaus and ensuring gradients do not vanish exponentially [33].

Observation 1 *For every n–qubit Hamiltonian $\hat{\mathcal{H}}$, every connected k–qubit region L, and every $\xi \in (0,1)$, there exists a kick strength $W \in [0, W^\star)$ inside the MBL phase such that the Floquet–initialized parameter set $\Theta_{\mathrm{prd}}(W)$ fulfils*

$$\mathbb{E}_{\boldsymbol{\vartheta}\in\Theta_{\mathrm{prd}}(W)} S_L < \xi S^{(\mathrm{Page})}(k,n). \tag{30}$$

Choosing $\xi < 1-\delta$ immediately violates Eq. (28) at that W.

Practically, this implies that initializing optimization within the MBL phase using sufficiently small kick strengths ensures gradients remain sufficiently large, effectively mitigating barren plateaus during early optimization stages.

Barren Plateaus– We numerically substantiate observation 1 by computing the initial gradients before optimization, $\nabla\langle\hat{\mathcal{H}}\rangle_{\boldsymbol{\vartheta}}$, for the Floquet initialization with varying W. The trial state is drawn from an ensemble of products of single-qubit Haar-random states, and $\hat{U}_t$ transforms the trial state into a computational basis state $|\varphi_c\rangle$. The energy associated with the initial parameters $\boldsymbol{\vartheta}$ is

$$\langle\hat{\mathcal{H}}\rangle_{\boldsymbol{\vartheta}} = \langle\varphi_c|\hat{U}^\dagger(\boldsymbol{\vartheta})\hat{U}_t\hat{\mathcal{H}}_{\mathrm{AA}}\hat{U}_t^\dagger\hat{U}(\boldsymbol{\vartheta})|\varphi_c\rangle. \tag{31}$$

For simplicity, we consider the critical point of the non-interacting Aubry-André model, setting $\alpha = (\sqrt{5}-1)/2$, $\phi = 0$, $J = 1$, $\Gamma = 0$, and $V = 2$. Fig. 3 plots the ℓ_∞-norm of the gradient as a function of W for various system sizes, averaged over 1000 samples per point. In the MBL phase, the gradients remain stable as n increases (though they decay with W), while in the thermal phase, the gradients decay exponentially with n, indicating the onset of barren plateaus. This gradient norm positively correlates with the deviation of $M_{t,k}$ from its Haar benchmark. Note that, although scale-independent points may appear within the MBL phase, they do not mark the precise transition to thermalization. Notably, most earlier studies characterize barren plateaus through the variance of the (zero-mean) gradient rather than its maximum component. In Appendix G we prove Proposition 2, which states that—under the usual zero-mean assumption—a non-negligible probability of observing a large ℓ_∞-gradient necessarily implies an inverse-polynomial lower bound on that variance.

Motivated by the information-preserving nature of the MBL phase, we define a uniform kick scaling operation and establish a theoretical lower bound on the gradient along a linear path connecting MBL- and thermally-initialized parameters.

Definition 2 (Uniform kick scaling) *Let $\boldsymbol{\vartheta} = (\boldsymbol{\vartheta}^{(1)}, \ldots, \boldsymbol{\vartheta}^{(D)}) \in \mathbb{R}^{D(m_s+m_k)}$ be a Floquet-initialized parameter point, i.e., $\boldsymbol{\vartheta}^{(\ell)} = \boldsymbol{\vartheta}^{(1)}$ for*

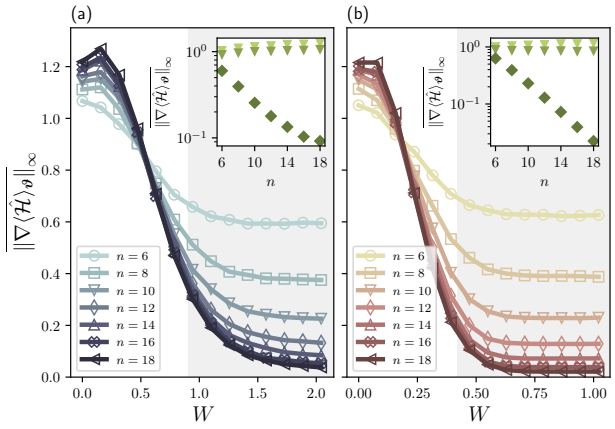


Figure 3: Visualization of the absence of barren plateaus in the MBL phase and their presence in the thermal phase after sampling the initial circuit parameters, analyzed using the target Hamiltonian $\hat{\mathcal{H}}_{\text{AA}}$ (defined in Eq. (27)). **(a)** ℓ_∞-norm of the energy gradient plotted as a function of kick strength W for a 1D ring topology. **(b)** ℓ_∞-norm of the energy gradient as a function of W for a $\text{Ci}_n(1,2)$ lattice topology. Insets illustrate the gradient scaling at various W values, emphasizing the contrast between the MBL phase (e.g., $W = 1/5, 2/5$ for the 1D ring and $W = 1/10, 1/5$ for the $\text{Ci}_n(1,2)$ topology) and the thermal phase (e.g., $W = 7/5$ for the 1D ring and $W = 7/10$ for the $\text{Ci}_n(1,2)$ topology). Darker green markers in the insets denote circuits with higher W.

all ℓ. m_s and m_k are the number of steady and kick parameters per layer, respectively. Given a scale factor $\lambda > 1$, we define the uniform kick scaling *operation as the map*

$$(\vartheta_j^{(\ell)})_{\ell=1}^D \longmapsto (\lambda\vartheta_j^{(\ell)})_{\ell=1}^D, \tag{32}$$

for all kick parameters j while leaving the steady parameters unchanged.

Theorem 3 *Let $U(\boldsymbol{\vartheta})$ be a depth-D layered circuit, Floquet-initialized at $\boldsymbol{\vartheta}_{\text{MBL}} \in \Theta_{\text{prd}}(W)$ with $W < W^\star$, and let $\hat{\mathcal{H}}$ be a Hermitian observable with $\|\hat{\mathcal{H}}\| \leq 1$. Let $\boldsymbol{\vartheta}_{\text{th}}$ be obtained by scaling all kick parameters of $\boldsymbol{\vartheta}_{\text{MBL}}$ by a factor $\lambda > 1$, and define the linear interpolation*

$$\gamma(s) := (1-s)\boldsymbol{\vartheta}_{\text{MBL}} + s\boldsymbol{\vartheta}_{\text{th}}, \quad s \in [0,1]. \tag{33}$$

If $\langle\hat{\mathcal{H}}\rangle_{\boldsymbol{\vartheta}_{\text{th}}}$ is exponentially small in n, and $D, m_k = \text{poly}(n)$, where m_k is the number of kick parameters per layer, then

$$\mathbb{E}_{s\in[0,1]} \left\|\nabla_{\boldsymbol{\vartheta}}\langle\hat{\mathcal{H}}\rangle(\gamma(s))\right\|_\infty \gtrsim \frac{|\langle\hat{\mathcal{H}}\rangle_{\boldsymbol{\vartheta}_{\text{MBL}}}|}{Dm_k(\lambda-1)W}, \tag{34}$$

which remains inverse-polynomial in n whenever $\langle\hat{\mathcal{H}}\rangle_{\boldsymbol{\vartheta}_{\text{MBL}}} = \Theta(1)$.

The proof for Theorem 3 is provided in Appendix H. This bound is meaningful in the MBL phase because its non-ergodic nature ensures the expectation value $\langle\hat{\mathcal{H}}\rangle_{\boldsymbol{\vartheta}_{\text{MBL}}}$ remains of order unity. In contrast, this expectation would be exponentially suppressed in the thermal phase, rendering the bound trivial.

Optimization– We proceed with the VQE optimization process by fixing the Hamiltonian parameters to $\alpha = (\sqrt{5}-1)/2$, $\phi = 0$, and $J = 1$. We employ the variational quantum eigensolver to prepare ground states of the one-dimensional $\hat{\mathcal{H}}_{\text{AA}}$ in different phases: non-interacting Anderson localized phase ($\Gamma = 0, V = 4$), extended phase ($\Gamma = 0, V = 1$), MBL phase ($\Gamma = 3, V = 6$), and ergodic phase ($\Gamma = 1, V = 2$). For the variational ansatz, we use a 1D ring connectivity square circuit with a depth $D = n$. We investigate three distinct initialization strategies as follows:

- MBL initialization: Floquet initialization with steady parameters uniformly sampled from $[-\pi, \pi)$ and kick parameters from $[-2/5, 2/5]$.
- Thermal initialization: Floquet initialization with steady parameters uniformly sampled from $[-\pi, \pi)$ and kick parameters from $[-7/5, 7/5]$.
- Random initialization: Each parameter in every layer uniformly sampled from $[-\pi, \pi)$.

We commence with a standard trial state $|\psi_t\rangle$ derived from an optimization of a low-dimensional matrix product state (MPS) featuring alternating bonds [88]. This MPS employs a bond dimension $\chi = 2$ between the $(2j-1)$-th and the $(2j)$-th tensors, and $\chi = 1$ between the $(2j)$-th and the $(2j+1)$-th tensors, for $j = 1, 2, \ldots, n/2$. The quantum state corresponding to this MPS configuration is

$$|\psi_t\rangle = \sum_{i_1,i_2,\ldots,i_n} \left[\prod_{j=1}^{n/2} A^{i_{2j-1},i_{2j}}\right] \left[\prod_{j=1}^{n/2-1} B^{i_{2j},i_{2j+1}}\right] |i_1, i_2, \ldots, i_n\rangle\,, \tag{35}$$

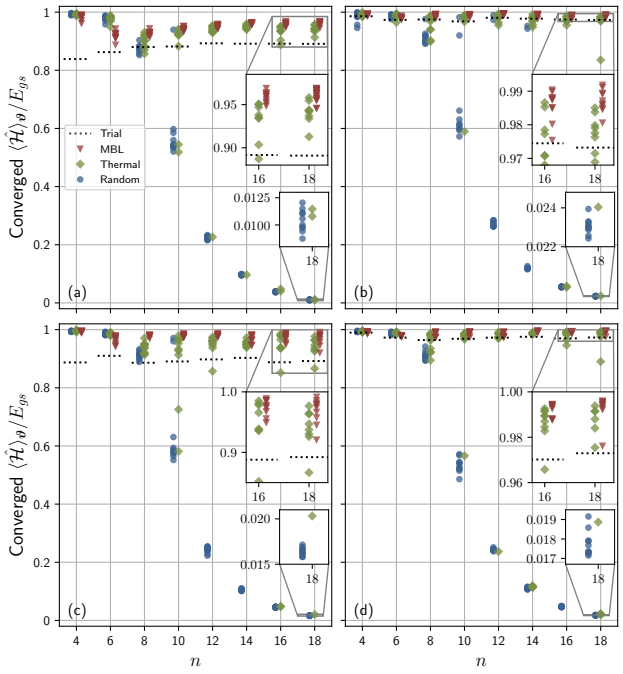


Figure 4: Converged approximation ratios from the variational quantum eigensolver for system sizes $n = 4, 6, 8, \ldots, 18$ across 10 samples of initial parameters. This comparison illustrates the superiority of the MBL initialization ($W = 2/5$, triangles) over thermal ($W = 7/5$, diamonds) and random (circles) strategies. Black dotted lines mark the trial state energy. **(a)** $\hat{\mathcal{H}}_{\text{AA}}$ in the extended phase ($\Gamma = 0, V = 1$). **(b)** $\hat{\mathcal{H}}_{\text{AA}}$ in the non-interacting Anderson localized phase ($\Gamma = 0, V = 4$). **(c)** $\hat{\mathcal{H}}_{\text{AA}}$ in the ergodic phase ($\Gamma = 1, V = 2$). **(d)** $\hat{\mathcal{H}}_{\text{AA}}$ in the MBL phase ($\Gamma = 3, V = 6$). The insets provide a zoomed view for large systems.

where $A^{i_{2j-1},i_{2j}}$ are 2×2 tensor matrices for bonds of dimension $\chi = 2$ and $B^{i_{2j-1},i_{2j}}$ are scalar values for bonds of dimension $\chi = 1$. These tensor parameters are tuned to minimize the trial energy $\langle\psi_t|\hat{\mathcal{H}}|\psi_t\rangle$. The resulting state $|\psi_t\rangle$ is subsequently transformed to a computational basis state $|\varphi_c\rangle$ using a shallow quantum circuit $\hat{U}_t$, constituted by $(n/2)$ two-qubit gates:

$$|\varphi_c\rangle = \hat{U}_t|\psi_t\rangle = \prod_{j=1}^{n/2} \hat{U}_{2j-1,2j}|\psi_t\rangle. \qquad (36)$$

For our computations, $|\varphi_c\rangle$ is selected as the computational basis state exhibiting the highest overlap with $|\psi_t\rangle$.

We proceed to the second stage: variational quantum optimization using a square circuit $\hat{U}(\boldsymbol{\vartheta})$. Initial parameters $\boldsymbol{\vartheta}$ are sampled according to the chosen initialization strategy, and optimization is performed via gradient descent with update rule $\boldsymbol{\vartheta} \leftarrow \boldsymbol{\vartheta} - \eta\nabla\langle\hat{\mathcal{H}}\rangle_{\boldsymbol{\vartheta}}$. The learning rate is set to $\eta = 0.05$ for Fig. 4(a–c) and $\eta = 0.01$ for (d). Optimization proceeds until the energy converges within a tolerance of 0.001 or a maximum of 1000 iterations is reached. Fig. 4 shows the ratio of the converged energy to the exact ground-state energy, averaged over 10 random initializations, as a function of system size and initialization scheme. MBL initialization consistently outperforms both thermal and random strategies, achieving approximation ratios close to unity across all Hamiltonian phases. In contrast, random initialization rapidly degrades with system size, often failing entirely for $n \gtrsim 14$, while thermal initialization performs moderately but inconsistently, occasionally producing low-energy states.

In addition to assessing initial gradients and final energies, our study is fundamentally focused on the optimization trajectory. We aim to ascertain whether MBL-based initializations can steer

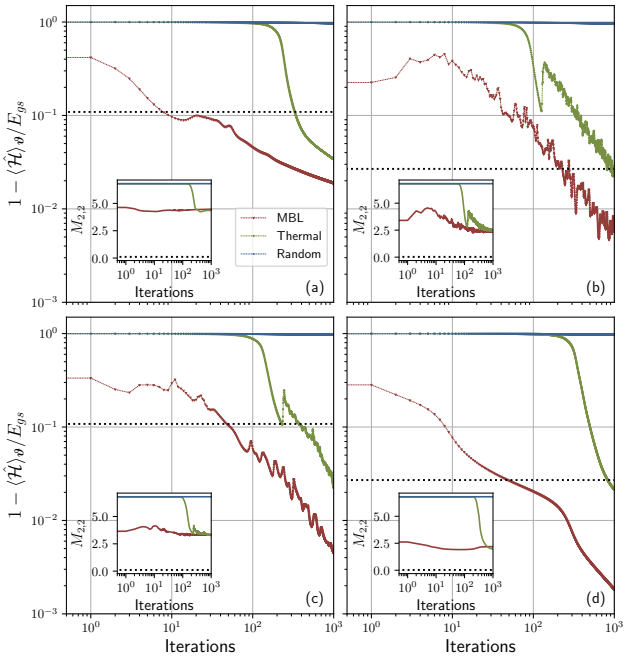


Figure 5: Relative energy error during optimization at $n = 18$, showing the rapid convergence of MBL initialization. **(a)** $\hat{\mathcal{H}}_{\text{AA}}$ in the non-interacting Anderson localized phase ($\Gamma = 0, V = 4$). **(b)** $\hat{\mathcal{H}}_{\text{AA}}$ in the extended phase ($\Gamma = 0, V = 1$). **(c)** $\hat{\mathcal{H}}_{\text{AA}}$ in the MBL phase ($\Gamma = 3, V = 6$). **(d)** $\hat{\mathcal{H}}_{\text{AA}}$ in the ergodic phase ($\Gamma = 1, V = 2$). Black dotted lines indicate the energy of the trial state prior to optimization. Insets show the low-weight stabilizer Rényi entropy $M_{2,2}$ throughout the optimization, emphasizing how initialization impacts energy convergence and entropy behaviors. Each curve corresponds to a random sample of initial parameters.

the optimization process towards more advantageous paths that prevent convergence to a random output state. Fig. 5 presents numerical results for the relative energy error and the low-weight stabilizer Rényi entropy $M_{2,2}$ throughout the optimization process for all four phases with a single instance of the initial circuit parameters. This visualization indicates that thermal initialization outperforms random initialization, which struggles to overcome barren plateaus and achieve lower energy states even after 1,000 iterations. The MBL initialization demonstrates performance superior to both, with the energy of the output state rapidly approaching that of the ground state. Furthermore, the $M_{2,2}$ trajectory underscores that when the circuit is initialized in the MBL phase, the output state remains far from its Haar benchmark throughout the optimization process. This behavior correlates with the absence of observed barren-plateau signatures and supports the enhanced efficiency and success probability of the variational optimization under MBL-based initialization.

5 Experimental Verification

In this section, we detail the experimental observation of the MBL to thermalization phase transition using Floquet-initialized variational quantum circuits on the `ibm_brisbane` quantum processor, a superconducting processor with 127 transmon qubits. Fig. 6(a) illustrates the architectural connectivity of the device, which includes 36 qubits of degree 3, 89 of degree 2, and 2 of degree 1. Table 1 lists the device's performance metrics, recorded during the experiments.

For clarity in our experimental setup, we focus on a specialized configuration of $\hat{\mathcal{H}}_{\mathrm{AA}}$ with parameters $J = 1$, $V = \Gamma = -2J$, $\alpha = 0$, and $\phi = \pi$. This setup corresponds to the ferromagnetic Heisenberg model, governed by the Hamiltonian:

$$\hat{\mathcal{H}}_{\mathrm{FH}} = -\frac{1}{2} \sum_{(i,j)\in \mathrm{edges}(G)} \left(\hat{\sigma}_i^x \hat{\sigma}_j^x + \hat{\sigma}_i^y \hat{\sigma}_j^y + \hat{\sigma}_i^z \hat{\sigma}_j^z \right). \tag{37}$$

This model is implemented on an intermittently coupled spin chain of n qubits, where alternate qubits are linked to an additional, isolated qubit, leading to non-uniform interactions across all spins. This configuration aligns well with the connectivity graph of the `ibm_brisbane` quantum processor. Notably, the circuit layout is dynamically optimized by the Qiskit compiler for $W = 1/2$ to enhance performance in practical experiments. In one of our experiments, this configuration is applied to 31 qubits, depicted in Fig. 6(a) with red circles representing qubits and connecting edges. The ground states of $\hat{\mathcal{H}}_{\mathrm{FH}}$ are reachable with a shallow circuit, allowing us to isolate the gradient-collapse signal at the MBL–thermalization crossover without conflating it with state-preparation complexity.

Before the experiment, we numerically simulate the system using a Floquet initialization strategy where the rotation angles within $\hat{\mathcal{R}}_x$, $\hat{\mathcal{R}}_{xx}$, and $\hat{\mathcal{R}}_{yy}$ are uniformly sampled from the

Parameter	Median Value
# of qubits	127
T_1	232.17μs
T_2	153.64μs
ECR error	7.802×10^{-3}
SX error	2.428×10^{-4}
Readout error	1.370×10^{-2}
Error per layered gate	1.9%

Table 1: Performance metrics of the `ibm_brisbane` quantum processor. Critical parameters include the number of qubits, coherence times (T_1 and T_2), error rates for echoed cross-resonance (ECR) gates and $\sqrt{X}$ (SX) gates, readout error, and the average error per gate in a layered circuit configuration.

Setup	**Qubits Used**
$n = 13$	Q_{73}, $Q_{82\text{–}86}$, Q_{92}, $Q_{101\text{–}105}$, Q_{111}.
$n = 19$	Q_{72}, $Q_{78\text{–}84}$, Q_{91}, Q_{92}, $Q_{97\text{–}99}$, $Q_{101\text{–}105}$, Q_{111}.
$n = 25$	Q_{72}, Q_{73}, $Q_{78\text{–}88}$, $Q_{91\text{–}93}$, $Q_{97\text{–}99}$, $Q_{103\text{–}107}$, Q_{111}.
$n = 31$	Q_{72}, Q_{73}, $Q_{78\text{–}88}$, $Q_{91\text{–}93}$, $Q_{95\text{–}99}$, $Q_{103\text{–}107}$, Q_{109}, Q_{111}, $Q_{121\text{–}123}$.

Table 2: Detailed qubits usage for different configurations with grouped subscript ranges

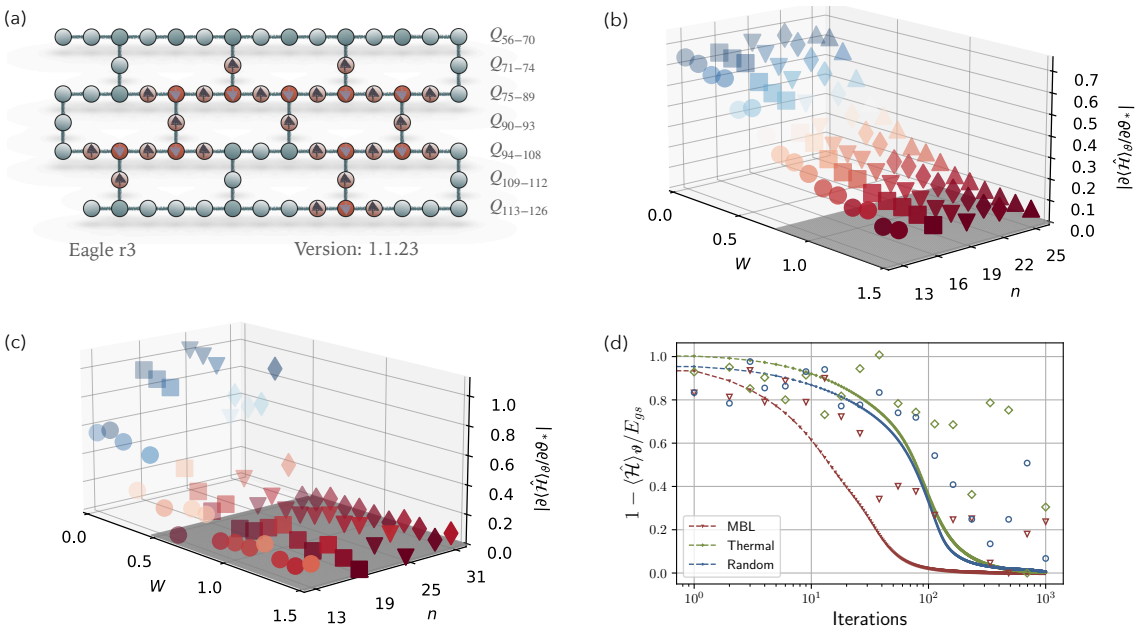


Figure 6: Experimental setup and analysis of the MBL–thermalization phase transition on IBM's `ibm_brisbane` quantum processor. **(a)** Qubit layout of `ibm_brisbane` alongside an intermittently coupled spin chain, represented by red circles (qubits) and connecting edges (couplings). Arrows indicate the initial alternating-spin Néel configuration. **(b)** Simulation results of the observed gradients of the Hamiltonian's expectation value as a function of the kick strength W for system sizes $n = 13, 16, 19, 21, 25$. **(c)** Experimental results of the observed gradients for system sizes $n = 13, 19, 25, 31$, with gradients similarly demonstrating decay patterns as W increases, indicating a phase transition at an experimentally adjusted point $W^\star \approx 1/2$. The experimental critical point is slightly shifted due to hardware noise. **(d)** Relative error during optimization shown numerically (lines) and experimentally (hollow markers) for system size $n = 19$.

range $[-W, W]$. Our analysis focuses on the Pauli-XX rotation at the center of the first layer of the spin chain, which has been verified to accurately represent the global trend observed across the entire gradient profile. A large gradient at a representative parameter (ϑ_*) empirically correlates with trainability of the full landscape. Considering our specific interest in observing phase transitions marked by the emergence and disappearance of significant gradients, we opt for a naive trial state in an alternating-spin Néel configuration, denoted as $|\psi_t\rangle = |\varphi_c\rangle = |\uparrow\rangle|\downarrow\rangle\cdots|\uparrow\rangle|\downarrow\rangle$, visually represented in Fig. 6(a). We measure the gradient of the Hamiltonian's expectation value relative to ϑ_* by executing each circuit configuration 4096 times. The circuit depth is set to $D = \lfloor (n-1)/6 \rfloor$ for a system with n qubits. The average absolute gradient, depicted in Fig. 6(b) for 200 samples of initial parameters, displays a clear phase transition from MBL to thermalization around a point of $W \approx 4/5$.

To initiate the experiment efficiently with limited resources, we employ a representative specialized sampling protocol for the initial Floquet circuit parameters, which includes all rotation angles within $\hat{\mathcal{R}}_x$, $\hat{\mathcal{R}}_z$, $\hat{\mathcal{R}}_{xx}$, $\hat{\mathcal{R}}_{yy}$, and $\hat{\mathcal{R}}_{zz}$. These parameters are generated using the zeros of the Chebyshev polynomial of the first kind, specifically:

$$\vartheta_j = \pi \cos\left(\frac{(2j-1)\pi}{2(m_s+m_k)}\right), \tag{38}$$

for $j = 1, 2, \ldots, m_s + m_k$, with $m_s = 2n$ and $m_k = 3n$, so that all angles initially lie in $[-\pi, \pi]$. We arrange these zeros in a staggered pattern, placing positive values at even indices and negative values at odd indices within the rotation-angle array. The angles assigned to $\hat{\mathcal{R}}_z$ and $\hat{\mathcal{R}}_{zz}$ are then kept fixed and play the role of the static steady disorder, while the angles in $\hat{\mathcal{R}}_x$, $\hat{\mathcal{R}}_{xx}$, and $\hat{\mathcal{R}}_{yy}$ are further rescaled by the kick strength W to ensure they fall within the range $[-W, W]$. Although this deterministic sampling deviates from the uniform randomness assumed in the theoretical analysis, it provides a representative set of disordered parameters that we expect to capture the essential features of the MBL–thermalization transition. Readout error mitigation is applied to enhance measurement accuracy, whereas gate er-

ror mitigation is intentionally omitted to preserve the intrinsic dynamics of the system.

The experiment is conducted across system sizes of $n = 13, 19, 25, 31$ using noisy physical qubits, as detailed in Table 2. As shown in Fig. 6(c), the observed absolute gradient values display a gradual decline in magnitude as the kick parameter W is increased, signaling a transition towards the thermal phase. Despite noise effects, an experimental critical transition point emerges near $W = 1/2$. Below this threshold, gradient magnitudes remain partially preserved. Notably, this experimental critical point is lower than the numerically predicted value $W = 4/5$, highlighting the impact of hardware noise on shifting the observed critical threshold. However, the experimental results still corroborate the general theoretical trend.

To more specifically illustrate the impact of the gradient on the optimization path, we plot the relative error throughout the optimization process for a system with $n = 19$ in Fig. 6(d). It displays both numerically simulated energy and experimental results (that have been rescaled for error mitigation) for several selected steps, using identical parameter sets. The circuit parameters are optimized classically. Compared to thermal and random initializations, the optimization employing MBL initialization demonstrates a rapid convergence towards the ground state. The improvement here is modest because this Hamiltonian is intentionally simple—our aim is to validate gradient revival experimentally, not to showcase a hard energy-minimization task. More demanding benchmarks, including assessments of classical MPS limitations on long-range models, comparisons with close-to-identity initialization to highlight escape from local minima, and robustness tests against trial-state perturbations and finite-shot noise, appear in Appendix I. These extensions demonstrate the protocol's practical advantages in challenging scenarios beyond the simple Heisenberg case.

6 Conclusions and Outlook

The primary motivation behind this research was to address the significant challenge of barren plateaus in variational quantum simulation, a phenomenon that considerably impedes the scalability and efficiency of quantum optimization. This investigation explored the transition from many-body localization (MBL) to thermalization within a universal variational quantum circuit framework. We introduced an MBL-based strategy aimed at mitigating excessive entanglement and thereby circumventing barren plateaus in variational quantum optimization. The application of this protocol led to marked enhancements in energy convergence for the Aubry-André model across various phases, promoting more efficient optimization processes. A significant aspect of our study was the experimental validation of the phase transition on the 127-qubit `ibm_brisbane` quantum processor through gradient computation. Moreover, this research innovates by utilizing barren plateaus as a novel metric for identifying the critical point of the MBL–thermalization phase transition. While our findings offer empirical evidence and establish a conditional bound on gradient magnitudes, we cannot rule out the emergence of barren plateaus at later stages of training.

Our results contribute to a deeper understanding of how MBL can mitigate barren plateaus in variational quantum optimization, consistent with insights from Ref. [37] regarding the relationship between barren plateaus and classical simulability. This alignment is particularly evident in the early stages of optimization, given the classical simulability of MBL systems [89]. Despite this, our methodology is intended to maintain substantial optimization gradients, even during a possible crossover to a thermal phase, thereby potentially enabling operation in regimes previously considered classically intractable. Warm-start analyses warn, however, that training will still fail unless one can initialize increasingly close to the relevant region of attraction as the system grows [38]. Furthermore, Ref. [39] shows that a polynomial-time classical surrogate of such a local patch can, in principle, be built after a moderate quantum data-acquisition stage. Whether such surrogates remain practical in our setting is an open—and important—question for future work.

This work opens several promising avenues for future research. One potential direction involves applying the MBL-based initialization protocol to quantum machine learning tasks, such as quantum generative adversarial networks [90]. Utilizing the unique properties of MBL systems could

potentially lead to more efficient and trainable quantum machine learning algorithms capable of generating distributions beyond the capabilities of classical methods. Further, exploring the interplay between MBL and other aspects of quantum circuits, such as measurement-induced phase transitions [31] and information scrambling [91], could yield valuable insights into quantum dynamics. Additionally, employing MBL in specialized variational quantum protocols, including QAOA variants [92–95] and the variational simulation of time evolution [96, 97], presents further exploration possibilities.

However, several open questions and potential enhancements persist within our framework. One critical issue is the selection of optimal trial states whose entanglement structures align closely with those of the target system's ground state. This alignment is crucial for enhancing the efficiency of quantum optimization but remains a complex challenge. While trial states from matrix product states can be compiled into log-depth shallow circuits [98–100], an alternative is the use of measurement-driven protocols to prepare highly entangled states in constant-depth, thus circumventing light-cone constraints [101–103]. Another significant consideration is the quantitative assessment of hardware noise effects on the critical points of MBL and thermalization phases. Fully understanding how this factor influences the transition points and the overall dynamics of variational quantum circuits is essential for enhancing their practical effectiveness. In parallel, MBL-based initialization is compatible with complementary post-processing strategies that mitigate algorithmic errors in quantum optimization, such as energy-extrapolation schemes [104]. Additionally, integrating MBL initialization with advanced techniques such as joint Bell measurements or circuit parallelism could significantly accelerate optimization processes [105, 106].

Acknowledgments

We are grateful to Luya Lou, Paul Skrzypczyk, Yunlong Yu, Tianyi Hao, Qihao Guo, Zheng-Hang Sun, B. Özguler, and M. Vavilov for insightful discussions. This work was supported by the Theory of Quantum Matter Unit, OIST. A part of this research was conducted while visiting the Okinawa Institute of Science and Technology (OIST) through the Theoretical Sciences Visiting Program (TSVP). We acknowledge the use of IBM Quantum services for this work.

References

[1] Alberto Peruzzo, Jarrod McClean, Peter Shadbolt, Man-Hong Yung, Xiao-Qi Zhou, Peter J. Love, Alán Aspuru-Guzik, and Jeremy L. O'Brien. "A variational eigenvalue solver on a photonic quantum processor". Nature Communications **5**, 4213 (2014).

[2] Dave Wecker, Matthew B. Hastings, and Matthias Troyer. "Progress towards practical quantum variational algorithms". Phys. Rev. A **92**, 042303 (2015).

[3] Edward Farhi, Jeffrey Goldstone, and Sam Gutmann. "A quantum approximate optimization algorithm" (2014). arXiv:1411.4028.

[4] Leo Zhou, Sheng-Tao Wang, Soonwon Choi, Hannes Pichler, and Mikhail D. Lukin. "Quantum approximate optimization algorithm: Performance, mechanism, and implementation on near-term devices". Phys. Rev. X **10**, 021067 (2020).

[5] Jarrod R. McClean, Sergio Boixo, Vadim N. Smelyanskiy, Ryan Babbush, and Hartmut Neven. "Barren plateaus in quantum neural network training landscapes". Nature Communications **9**, 4812 (2018).

[6] Carlos Ortiz Marrero, Mária Kieferová, and Nathan Wiebe. "Entanglement-induced barren plateaus". PRX Quantum **2**, 040316 (2021).

[7] Martin Larocca, Piotr Czarnik, Kunal Sharma, Gopikrishnan Muraleedharan, Patrick J. Coles, and M. Cerezo. "Diagnosing Barren Plateaus with Tools from Quantum Optimal Control". Quantum **6**, 824 (2022).

[8] Enrique Cervero Martín, Kirill Plekhanov, and Michael Lubasch. "Barren plateaus in quantum tensor network optimization". Quantum **7**, 974 (2023).

[9] Martín Larocca, Supanut Thanasilp, Samson Wang, Kunal Sharma, Jacob Biamonte, Patrick J. Coles, Lukasz Cincio, Jarrod R. McClean, Zoë Holmes, and M. Cerezo. "Barren plateaus in variational quantum computing". Nature Reviews Physics **7**, 174–189 (2025).

[10] Michael Ragone, Bojko N. Bakalov, Frédéric Sauvage, Alexander F. Kemper, Carlos Ortiz Marrero, Martín Larocca, and M. Cerezo. "A lie algebraic theory of barren plateaus for deep parameterized quantum circuits". Nature Communications **15**, 7172 (2024).

[11] Enrico Fontana, Dylan Herman, Shouvanik Chakrabarti, Niraj Kumar, Romina Yalovetzky, Jamie Heredge, Shree Hari Sureshbabu, and Marco Pistoia. "Characterizing barren plateaus in quantum ansätze with the adjoint representation". Nature Communications **15**, 7171 (2024).

[12] Eric R. Anschuetz and Bobak T. Kiani. "Quantum variational algorithms are swamped with traps". Nature Communications **13**, 7760 (2022).

[13] Eric R. Anschuetz. "A unified theory of quantum neural network loss landscapes" (2025). arXiv:2408.11901.

[14] Chenfeng Cao, Filippo Maria Gambetta, Ashley Montanaro, and Raul A. Santos. "Unveiling quantum phase transitions from traps in variational quantum algorithms". npj Quantum Information **11**, 93 (2025).

[15] Antonio Anna Mele, Armando Angrisani, Soumik Ghosh, Sumeet Khatri, Jens Eisert, Daniel Stilck França, and Yihui Quek. "Noise-induced shallow circuits and absence of barren plateaus" (2024). arXiv:2403.13927.

[16] Samson Wang, Enrico Fontana, M. Cerezo, Kunal Sharma, Akira Sone, Lukasz Cincio, and Patrick J. Coles. "Noise-induced barren plateaus in variational quantum algorithms". Nature Communications **12**, 6961 (2021).

[17] Yihui Quek, Daniel Stilck França, Sumeet Khatri, Johannes Jakob Meyer, and Jens Eisert. "Exponentially tighter bounds on limitations of quantum error mitigation". Nature Physics **20**, 1648–1658 (2024).

[18] Daniel Stilck França and Raul García-Patrón. "Limitations of optimization algorithms on noisy quantum devices". Nature Physics **17**, 1221–1227 (2021).

[19] M. Cerezo, Guillaume Verdon, Hsin-Yuan Huang, Lukasz Cincio, and Patrick J. Coles. "Challenges and opportunities in quantum machine learning". Nature Computational Science **2**, 567–576 (2022).

[20] D. Gross, S. T. Flammia, and J. Eisert. "Most quantum states are too entangled to be useful as computational resources". Phys. Rev. Lett. **102**, 190501 (2009).

[21] H. J. Briegel, D. E. Browne, W. Dür, R. Raussendorf, and M. Van den Nest. "Measurement-based quantum computation". Nature Physics **5**, 19–26 (2009).

[22] Andrew Arrasmith, M. Cerezo, Piotr Czarnik, Lukasz Cincio, and Patrick J. Coles. "Effect of barren plateaus on gradient-free optimization". Quantum **5**, 558 (2021).

[23] Andrew Arrasmith, Zoë Holmes, M Cerezo, and Patrick J Coles. "Equivalence of quantum barren plateaus to cost concentration and narrow gorges". Quantum Science and Technology **7**, 045015 (2022).

[24] M. Cerezo, Akira Sone, Tyler Volkoff, Lukasz Cincio, and Patrick J. Coles. "Cost function dependent barren plateaus in shallow parametrized quantum circuits". Nature Communications **12**, 1791 (2021).

[25] Hao-Kai Zhang, Shuo Liu, and Shi-Xin Zhang. "Absence of barren plateaus in finite local-depth circuits with long-range entanglement". Phys. Rev. Lett. **132**, 150603 (2024).

[26] Roeland Wiersema, Cunlu Zhou, Yvette de Sereville, Juan Felipe Carrasquilla, Yong Baek Kim, and Henry Yuen. "Exploring entanglement and optimization within the Hamiltonian variational ansatz". PRX Quantum **1**, 020319 (2020).

[27] Arthur Pesah, M. Cerezo, Samson Wang, Tyler Volkoff, Andrew T. Sornborger, and Patrick J. Coles. "Absence of barren plateaus in quantum convolutional neural networks". Phys. Rev. X **11**, 041011 (2021).

[28] Chen Zhao and Xiao-Shan Gao. "Analyzing the barren plateau phenomenon in training quantum neural networks with the ZX-calculus". Quantum **5**, 466 (2021).

[29] Chae-Yeun Park and Nathan Killoran. "Hamiltonian variational ansatz without barren plateaus". Quantum **8**, 1239 (2024).

[30] Xin Wang, Bo Qi, Yabo Wang, and Daoyi Dong. "Entanglement-variational hardware-efficient ansatz for eigensolvers". Phys. Rev. Appl. **21**, 034059 (2024).

[31] Roeland Wiersema, Cunlu Zhou, Juan Felipe Carrasquilla, and Yong Baek Kim. "Measurement-induced entanglement phase transitions in variational quantum circuits". SciPost Phys. **14**, 147 (2023).

[32] Antonio A. Mele, Glen B. Mbeng, Giuseppe E. Santoro, Mario Collura, and Pietro Torta. "Avoiding barren plateaus via transferability of smooth solutions in a Hamiltonian variational ansatz". Phys. Rev. A **106**, L060401 (2022).

[33] Stefan H. Sack, Raimel A. Medina, Alexios A. Michailidis, Richard Kueng, and Maksym Serbyn. "Avoiding barren plateaus using classical shadows". PRX Quantum **3**, 020365 (2022).

[34] Ricard Puig, Marc Drudis, Supanut Thanasilp, and Zoë Holmes. "Variational quantum simulation: A case study for understanding warm starts". PRX Quantum **6**, 010317 (2025).

[35] Taylor L. Patti, Khadijeh Najafi, Xun Gao, and Susanne F. Yelin. "Entanglement devised barren plateau mitigation". Phys. Rev. Res. **3**, 033090 (2021).

[36] Yabo Wang, Bo Qi, Chris Ferrie, and Daoyi Dong. "Trainability enhancement of parameterized quantum circuits via reduced-domain parameter initialization". Phys. Rev. Appl. **22**, 054005 (2024).

[37] M. Cerezo, Martin Larocca, Diego García-Martín, N. L. Diaz, Paolo Braccia, Enrico Fontana, Manuel S. Rudolph, Pablo Bermejo, Aroosa Ijaz, Supanut Thanasilp, Eric R. Anschuetz, and Zoë Holmes. "Does provable absence of barren plateaus imply classical simulability?". Nature Communications **16**, 7907 (2025).

[38] Hela Mhiri, Ricard Puig, Sacha Lerch, Manuel S. Rudolph, Thiparat Chotibut, Supanut Thanasilp, and Zoë Holmes. "A unifying account of warm start guarantees for patches of quantum landscapes" (2025). arXiv:2502.07889.

[39] Sacha Lerch, Ricard Puig, Manuel S. Rudolph, Armando Angrisani, Tyson Jones, M. Cerezo, Supanut Thanasilp, and Zoë Holmes. "Efficient quantum-enhanced classical simulation for patches of quantum landscapes" (2024). arXiv:2411.19896.

[40] P. W. Anderson. "Absence of diffusion in certain random lattices". Phys. Rev. **109**, 1492–1505 (1958).

[41] D.M. Basko, I.L. Aleiner, and B.L. Altshuler. "Metal–insulator transition in a weakly interacting many-electron system with localized single-particle states". Annals of Physics **321**, 1126–1205 (2006).

[42] Rahul Nandkishore and David A. Huse. "Many-body localization and thermalization in quantum statistical mechanics". Annual Review of Condensed Matter Physics **6**, 15–38 (2015).

[43] Dmitry A. Abanin, Ehud Altman, Immanuel Bloch, and Maksym Serbyn. "Colloquium: Many-body localization, thermalization, and entanglement". Rev. Mod. Phys. **91**, 021001 (2019).

[44] Piotr Sierant, Maciej Lewenstein, Antonello Scardicchio, Lev Vidmar, and Jakub Zakrzewski. "Many-body localization in the age of classical computing*". Reports on Progress in Physics **88**, 026502 (2025).

[45] J. Eisert, M. Cramer, and M. B. Plenio. "Colloquium: Area laws for the entanglement entropy". Rev. Mod. Phys. **82**, 277–306 (2010).

[46] Chenfeng Cao, Jian Xue, Nic Shannon, and Robert Joynt. "Speedup of the quantum adiabatic algorithm using delocalization catalysis". Phys. Rev. Res. **3**, 013092 (2021).

[47] Shuo Liu, Shi-Xin Zhang, Chang-Yu Hsieh, Shengyu Zhang, and Hong Yao. "Probing many-body localization by excited-state variational quantum eigensolver". Phys. Rev. B **107**, 024204 (2023).

[48] Jirawat Tangpanitanon, Supanut Thanasilp, Ninnat Dangniam, Marc-Antoine Lemonde, and

Dimitris G. Angelakis. “Expressibility and trainability of parametrized analog quantum systems for machine learning applications”. Phys. Rev. Res. **2**, 043364 (2020).

[49] Kaixiang Su and Michael J. Lawler. “Signatures of interacting floquet phases in shallow quantum circuits”. Phys. Rev. B **106**, 214310 (2022).

[50] D. Zhu, S. Johri, N. H. Nguyen, C. Huerta Alderete, K. A. Landsman, N. M. Linke, C. Monroe, and A. Y. Matsuura. “Probing many-body localization on a noisy quantum computer”. Phys. Rev. A **103**, 032606 (2021).

[51] Oles Shtanko, Derek S. Wang, Haimeng Zhang, Nikhil Harle, Alireza Seif, Ramis Movassagh, and Zlatko Minev. “Uncovering local integrability in quantum many-body dynamics”. Nature Communications **16**, 2552 (2025).

[52] Chae-Yeun Park, Minhyeok Kang, and Joonsuk Huh. “Hardware-efficient ansatz without barren plateaus in any depth” (2024). arXiv:2403.04844.

[53] Kasidit Srimahajariyapong, Supanut Thanasilp, and Thiparat Chotibut. “Connecting phases of matter to the flatness of the loss landscape in analog variational quantum algorithms” (2025). arXiv:2506.13865.

[54] Pedro Ponte, Z. Papić, Fran çois Huveneers, and Dmitry A. Abanin. “Many-body localization in periodically driven systems”. Phys. Rev. Lett. **114**, 140401 (2015).

[55] Achilleas Lazarides, Arnab Das, and Roderich Moessner. “Fate of many-body localization under periodic driving”. Phys. Rev. Lett. **115**, 030402 (2015).

[56] Dmitry A. Abanin, Wojciech De Roeck, and François Huveneers. “Theory of many-body localization in periodically driven systems”. Annals of Physics **372**, 1–11 (2016).

[57] D. R. Hartree. “The wave mechanics of an atom with a non-coulomb central field. part i. theory and methods”. Mathematical Proceedings of the Cambridge Philosophical Society **24**, 89–110 (1928).

[58] F. Verstraete, V. Murg, and J.I. Cirac. “Matrix product states, projected entangled pair states, and variational renormalization group methods for quantum spin systems”. Advances in Physics **57**, 143–224 (2008).

[59] Ulrich Schollwöck. “The density-matrix renormalization group in the age of matrix product states”. Annals of Physics **326**, 96–192 (2011).

[60] Liangsheng Zhang, Vedika Khemani, and David A. Huse. “A floquet model for the many-body localization transition”. Phys. Rev. B **94**, 224202 (2016).

[61] Takashi Mori, Tomotaka Kuwahara, and Keiji Saito. “Rigorous bound on energy absorption and generic relaxation in periodically driven quantum systems”. Phys. Rev. Lett. **116**, 120401 (2016).

[62] Dmitry A. Abanin, Wojciech De Roeck, Wen Wei Ho, and Fran çois Huveneers. “Effective hamiltonians, prethermalization, and slow energy absorption in periodically driven many-body systems”. Phys. Rev. B **95**, 014112 (2017).

[63] Takashi Mori, Tatsuhiko N Ikeda, Eriko Kaminishi, and Masahito Ueda. “Thermalization and prethermalization in isolated quantum systems: a theoretical overview”. Journal of Physics B: Atomic, Molecular and Optical Physics **51**, 112001 (2018).

[64] Kaining Zhang, Liu Liu, Min-Hsiu Hsieh, and Dacheng Tao. “Escaping from the barren plateau via gaussian initializations in deep variational quantum circuits”. In S. Koyejo, S. Mohamed, A. Agarwal, D. Belgrave, K. Cho, and A. Oh, editors, Advances in Neural Information Processing Systems. Volume 35, pages 18612–18627. Curran Associates, Inc. (2022).

[65] Zoë Holmes, Kunal Sharma, M. Cerezo, and Patrick J. Coles. “Connecting ansatz expressibility to gradient magnitudes and barren plateaus”. PRX Quantum **3**, 010313 (2022).

[66] Joseph M. Renes, Robin Blume-Kohout, A. J. Scott, and Carlton M. Caves. “Symmetric informationally complete quantum measurements”. Journal of Mathematical Physics **45**, 2171–2180 (2004).

[67] D. Gross, K. Audenaert, and J. Eisert. “Evenly distributed unitaries: On the structure of unitary designs”. Journal of Mathematical Physics**48** (2007).

[68] Christoph Dankert, Richard Cleve, Joseph Emerson, and Etera Livine. "Exact and approximate unitary 2-designs and their application to fidelity estimation". Phys. Rev. A **80**, 012304 (2009).

[69] John Watrous. "The theory of quantum information". Cambridge University Press. (2018).

[70] Antonio Anna Mele. "Introduction to Haar Measure Tools in Quantum Information: A Beginner's Tutorial". Quantum **8**, 1340 (2024).

[71] Benoît Collins and Piotr Śniady. "Integration with respect to the haar measure on unitary, orthogonal and symplectic group". Communications in Mathematical Physics **264**, 773–795 (2006).

[72] Luca D'Alessio and Marcos Rigol. "Long-time behavior of isolated periodically driven interacting lattice systems". Phys. Rev. X **4**, 041048 (2014).

[73] A. De Luca and A. Scardicchio. "Ergodicity breaking in a model showing many-body localization". Europhysics Letters **101**, 37003 (2013).

[74] David J. Luitz, Xavier Plat, Fabien Alet, and Nicolas Laflorencie. "Universal logarithmic corrections to entanglement entropies in two dimensions with spontaneously broken continuous symmetries". Phys. Rev. B **91**, 155145 (2015).

[75] Sukin Sim, Peter D. Johnson, and Alán Aspuru-Guzik. "Expressibility and entangling capability of parameterized quantum circuits for hybrid quantum-classical algorithms". Advanced Quantum Technologies **2**, 1900070 (2019).

[76] Aram W. Harrow. "The church of the symmetric subspace" (2013). arXiv:1308.6595.

[77] Arijeet Pal and David A. Huse. "Many-body localization phase transition". Phys. Rev. B **82**, 174411 (2010).

[78] Lorenzo Leone, Salvatore F. E. Oliviero, and Alioscia Hamma. "Stabilizer rényi entropy". Phys. Rev. Lett. **128**, 050402 (2022).

[79] Salvatore F. E. Oliviero, Lorenzo Leone, and Alioscia Hamma. "Magic-state resource theory for the ground state of the transverse-field ising model". Phys. Rev. A **106**, 042426 (2022).

[80] Davide Rattacaso, Lorenzo Leone, Salvatore F. E. Oliviero, and Alioscia Hamma. "Stabilizer entropy dynamics after a quantum quench". Phys. Rev. A **108**, 042407 (2023).

[81] Nikolas P. Breuckmann and Jens Niklas Eberhardt. "Quantum low-density parity-check codes". PRX Quantum **2**, 040101 (2021).

[82] Don N. Page. "Average entropy of a subsystem". Phys. Rev. Lett. **71**, 1291–1294 (1993).

[83] S. K. Foong and S. Kanno. "Proof of page's conjecture on the average entropy of a subsystem". Phys. Rev. Lett. **72**, 1148–1151 (1994).

[84] M B Hastings. "An area law for one-dimensional quantum systems". Journal of Statistical Mechanics: Theory and Experiment **2007**, P08024 (2007).

[85] Serge Aubry and Gilles André. "Analyticity breaking and anderson localization in incommensurate lattices". Ann. Israel Phys. Soc **3**, 18 (1980).

[86] Shankar Iyer, Vadim Oganesyan, Gil Refael, and David A. Huse. "Many-body localization in a quasiperiodic system". Phys. Rev. B **87**, 134202 (2013).

[87] P. Jordan and E. Wigner. "Über das paulische äquivalenzverbot". Zeitschrift für Physik **47**, 631–651 (1928).

[88] Román Orús. "Tensor networks for complex quantum systems". Nature Reviews Physics **1**, 538–550 (2019).

[89] Guifré Vidal. "Efficient simulation of one-dimensional quantum many-body systems". Phys. Rev. Lett. **93**, 040502 (2004).

[90] Christa Zoufal, Aurélien Lucchi, and Stefan Woerner. "Quantum generative adversarial networks for learning and loading random distributions". npj Quantum Information **5**, 103 (2019).

[91] Xiao Mi et al. "Information scrambling in quantum circuits". Science **374**, 1479–1483 (2021).

[92] Yunlong Yu, Chenfeng Cao, Carter Dewey, Xiang-Bin Wang, Nic Shannon, and Robert Joynt. "Quantum approximate optimization algorithm with adaptive bias fields". Phys. Rev. Res. **4**, 023249 (2022).

[93] Yunlong Yu, Chenfeng Cao, Xiang-Bin Wang, Nic Shannon, and Robert Joynt. "Solution of sat problems with the adaptive-bias quantum approximate optimization algorithm". Phys. Rev. Res. **5**, 023147 (2023).

[94] Yunlong Yu, Xiang-Bin Wang, Nic Shannon, and Robert Joynt. "Warm-start adaptive-bias quantum approximate optimization algorithm". Phys. Rev. A **112**, 012422 (2025).

[95] Zheng-Hang Sun, Yong-Yi Wang, Jian Cui, and Heng Fan. "Improving the performance of quantum approximate optimization for preparing non-trivial quantum states without translational symmetry". New Journal of Physics **25**, 013015 (2023).

[96] Xiao Yuan, Suguru Endo, Qi Zhao, Ying Li, and Simon C. Benjamin. "Theory of variational quantum simulation". Quantum **3**, 191 (2019).

[97] Marcello Benedetti, Mattia Fiorentini, and Michael Lubasch. "Hardware-efficient variational quantum algorithms for time evolution". Phys. Rev. Res. **3**, 033083 (2021).

[98] Shi-Ju Ran. "Encoding of matrix product states into quantum circuits of one- and two-qubit gates". Phys. Rev. A **101**, 032310 (2020).

[99] Manuel S Rudolph, Jing Chen, Jacob Miller, Atithi Acharya, and Alejandro Perdomo-Ortiz. "Decomposition of matrix product states into shallow quantum circuits". Quantum Science and Technology **9**, 015012 (2023).

[100] Daniel Malz, Georgios Styliaris, Zhi-Yuan Wei, and J. Ignacio Cirac. "Preparation of matrix product states with log-depth quantum circuits". Phys. Rev. Lett. **132**, 040404 (2024).

[101] Elisa Bäumer, Vinay Tripathi, Derek S. Wang, Patrick Rall, Edward H. Chen, Swarnadeep Majumder, Alireza Seif, and Zlatko K. Minev. "Efficient long-range entanglement using dynamic circuits". PRX Quantum **5**, 030339 (2024).

[102] Rahul Sahay and Ruben Verresen. "Finite-depth preparation of tensor network states from measurement" (2024). arXiv:2404.17087.

[103] Chenfeng Cao and Jens Eisert. "Measurement-driven quantum advantages in shallow circuits" (2025). arXiv:2505.04705.

[104] Chenfeng Cao, Yunlong Yu, Zipeng Wu, Nic Shannon, Bei Zeng, and Robert Joynt. "Mitigating algorithmic errors in quantum optimization through energy extrapolation". Quantum Science and Technology **8**, 015004 (2022).

[105] Chenfeng Cao, Hiroshi Yano, and Yuya O. Nakagawa. "Accelerated variational quantum eigensolver with joint bell measurement". Phys. Rev. Res. **6**, 013205 (2024).

[106] Lana Mineh and Ashley Montanaro. "Accelerating the variational quantum eigensolver using parallelism". Quantum Science and Technology **8**, 035012 (2023).

[107] Robert R. Tucci. "An introduction to cartan's kak decomposition for qc programmers" (2005). arXiv:quant-ph/0507171.

[108] A Yu Kitaev. "Quantum computations: algorithms and error correction". Russian Mathematical Surveys **52**, 1191 (1997).

[109] S. Datta, S. Howard, and Douglas Cochran. "Geometry of the welch bounds". Linear Algebra and Its Applications **437**, 2455–2470 (2012).

[110] Richard N. Youngworth, Benjamin B. Gallagher, and Brian L. Stamper. "An overview of power spectral density (PSD) calculations". In H. Philip Stahl, editor, Optical Manufacturing and Testing VI. Volume 5869, page 58690U. International Society for Optics and PhotonicsSPIE (2005).

[111] Steven R. White. "Density matrix formulation for quantum renormalization groups". Phys. Rev. Lett. **69**, 2863–2866 (1992).

[112] Diederik P. Kingma and Jimmy Ba. "Adam: A method for stochastic optimization" (2017). arXiv:1412.6980.

[113] Abhinav Kandala, Antonio Mezzacapo, Kristan Temme, Maika Takita, Markus Brink, Jerry M. Chow, and Jay M. Gambetta. "Hardware-efficient variational quantum eigensolver for small molecules and quantum magnets". Nature **549**, 242–246 (2017).

[114] Ophelia Crawford, Barnaby van Straaten, Daochen Wang, Thomas Parks, Earl Campbell, and Stephen Brierley. "Efficient quantum measurement of Pauli operators in the presence of finite sampling error". Quantum **5**, 385 (2021).

Appendices

A Proof of Circuit Universality

Proposition 1 (Circuit universality) *The sequential layered variational circuit in Fig. 1 is universal: for any $U \in \mathrm{SU}(2^n)$ and any $\varepsilon > 0$, there exist parameters $\boldsymbol{\vartheta}$ such that the unitary $\hat{U}(\boldsymbol{\vartheta})$ satisfies*

$$\left\|\hat{U}(\boldsymbol{\vartheta}) - U\right\|_\infty \leq \varepsilon, \tag{39}$$

with circuit depth exponential in n and polylogarithmic in $1/\varepsilon$. Moreover, if U admits a nearest-neighbor decomposition with $\mathrm{poly}(n, \log(1/\varepsilon))$ layers of two-qubit gates, the same accuracy can be achieved with depth $D = \mathrm{poly}(n, \log(1/\varepsilon))$.

Proof Consider any pair of adjacent qubits, denoted as Q_j and Q_k. We can construct a layout with 15 parameterized gates in three consecutive layers, as depicted in Fig. 7. It is known that any single-qubit unitary operation can be achieved through consecutive rotations of Pauli-$Z - X - Z$ or Pauli-$X - Z - X$, up to a global phase. Moreover, the operation

$$\exp\left(-i\frac{\vartheta_{xx}}{2}\hat{\sigma}_j^x\hat{\sigma}_k^x\right)\exp\left(-i\frac{\vartheta_{yy}}{2}\hat{\sigma}_j^y\hat{\sigma}_k^y\right)\exp\left(-i\frac{\vartheta_{zz}}{2}\hat{\sigma}_j^z\hat{\sigma}_k^z\right) \tag{40}$$

is equivalent to the operation

$$\exp\left(-i\frac{\vartheta_{xx}}{2}\hat{\sigma}_j^x\hat{\sigma}_k^x - i\frac{\vartheta_{yy}}{2}\hat{\sigma}_j^y\hat{\sigma}_k^y - i\frac{\vartheta_{zz}}{2}\hat{\sigma}_j^z\hat{\sigma}_k^z\right). \tag{41}$$

Consequently, we can employ Cartan's KAK decomposition [107]:

$$\begin{aligned}\hat{U}(\boldsymbol{\vartheta}) =& \hat{U}_s(\vartheta_1,\vartheta_2,\vartheta_3)\otimes\hat{U}_s(\vartheta_4,\vartheta_5,\vartheta_6)\exp\left(-i\frac{\vartheta_7}{2}\hat{\sigma}_j^x\hat{\sigma}_k^x - i\frac{\vartheta_8}{2}\hat{\sigma}_j^y\hat{\sigma}_k^y - i\frac{\vartheta_9}{2}\hat{\sigma}_j^z\hat{\sigma}_k^z\right)\\ &\cdot\hat{U}_s(\vartheta_{10},\vartheta_{11},\vartheta_{12})\otimes\hat{U}_s(\vartheta_{13},\vartheta_{14},\vartheta_{15}),\end{aligned} \tag{42}$$

where $\hat{U}_s(\vartheta_\alpha,\vartheta_\beta,\vartheta_\gamma)$ represents a 3-parameter universal single-qubit unitary acting on Q_j or Q_k. Any two-qubit unitary operation $\hat{U} \in \mathrm{SU}(4)$ can be decomposed into the KAK form. As a result, we can implement arbitrary 1-qubit and 2-qubit gates, such as the universal gate set $\{\mathrm{CNOT}, \mathrm{H}, \mathrm{S}, \mathrm{T}\}$.

A nearest-neighbour SWAP network of depth $\mathcal{O}(n)$ brings any two qubits adjacent. Applying the Solovay–Kitaev theorem [108] then ensures an approximation within ε, with an overall circuit depth exponential in n and polylogarithmic in $1/\varepsilon$.

If U already admits a nearest-neighbour decomposition with $\mathrm{poly}(n, \log(1/\varepsilon))$ layers, the same reasoning directly yields depth $D = \mathcal{O}(\mathrm{poly}(n, \log(1/\varepsilon)))$. ■

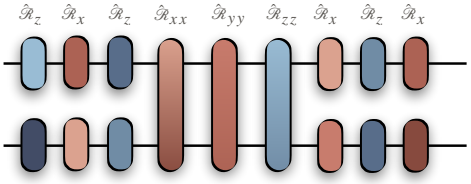


Figure 7: Cartan's KAK decomposition of arbitrary double-qubit unitary $U \in \mathrm{SU}(4)$. The diagram illustrates a constructive decomposition of a general two-qubit unitary into 15 parameterized gates: local Euler rotations and a central block of XX, YY, and ZZ interactions.

B Level-statistics confirmation of CUE

To determine the appropriate random-matrix ensemble characterizing the thermal phase of our Floquet-initialized circuits, we conduct a level-statistics analysis of the quasienergies. Starting from Poisson (MBL) statistics at small kick strength W, the spectra change towards the circular unitary ensemble (CUE) as W increases, signaling ergodicity and level repulsion.

The principal diagnostic is the disorder-averaged adjacent-gap ratio

$$\langle r\rangle := \langle \frac{\min(\delta_i, \delta_{i+1})}{\max(\delta_i, \delta_{i+1})} \rangle \tag{43}$$

where δ_i represents the spacing between consecutive quasienergy levels (eigenphases of the Floquet unitary). For Poisson statistics, $\langle r\rangle \approx 0.386$; for the circular orthogonal ensemble (COE), $\langle r\rangle \approx 0.536$; and for the circular unitary ensemble (CUE), $\langle r\rangle \approx 0.603$.

For $n = 6, 8, 10, 12$ qubits we diagonalized the Floquet unitary in both the one-D ring and the circulant graph $\mathrm{Ci}_n(1, 2)$ topologies. Fig. 8 shows $\langle r\rangle$ versus W: all curves cross over from the Poisson plateau at small W to the CUE plateau at large W, with the transition sharpening as n grows. In the thermal regime we obtain $\langle r\rangle \simeq 0.60$, fully consistent with CUE and incompatible with COE. This behaviour is expected because our ansatz employs non-commuting rotations with complex phases, thereby breaking time-reversal symmetry and generating the full Lie algebra $\mathfrak{su}(2^n)$. In this work, we pinpoint the MBL–thermalization phase transition using metrics such as the inverse participation ratio, entanglement entropy, and low-weight stabilizer Rényi entropy (as detailed in the main text), rather than level statistics. These measures are more closely linked to variational quantum algorithm (VQA) trainability, entanglement scaling, and localization properties, and prove computationally efficient for the studied system sizes, circumventing the requirement for full spectral diagonalization.

Even if the thermal phase were governed by COE (e.g., for real-valued gates yielding unitaries in the orthogonal group $\mathcal{O}(d)$ with $d = 2^n$), our t-design-based diagnostics would hold. The moments of COE and CUE are asymptotically equivalent, with discrepancies manifesting only as sub-leading terms in the Weingarten expansion [71]. Concretely, for fixed order t and large d,

$$\int_{\mathrm{O}(d)} O^{\otimes t} \otimes O^{\dagger\otimes t} d\mu_{\mathrm{O}}(O) = \int_{\mathrm{U}(d)} U^{\otimes t} \otimes U^{\dagger\otimes t} d\mu_{\mathrm{U}}(U) + \mathcal{O}\left(\frac{1}{d}\right), \tag{44}$$

where μ_{O} and μ_{U} denote the respective Haar measures. Thus, applying a COE unitary to a fixed computational basis state generates an orthogonal t-design, with differences vanishing for large systems and absent from our normalized metrics.

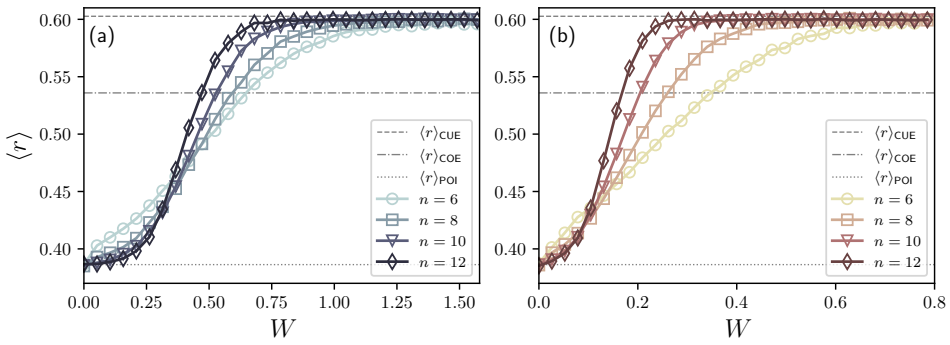


Figure 8: Disorder-averaged adjacent-gap ratio $\langle r\rangle$ versus kick strength W for system sizes $n = 6, 8, 10, 12$. **(a)** One-dimensional ring connectivity. **(b)** Circulant graph $\mathrm{Ci}_n(1, 2)$. Horizontal dashed lines (from top to bottom) mark the universal CUE ($\langle r\rangle \simeq 0.603$), COE ($\langle r\rangle \simeq 0.536$), and Poisson ($\langle r\rangle \simeq 0.386$) benchmarks. The crossover of the numerical curves from the Poisson plateau at small W to the CUE plateau at large W signals the many-body-localization-to-thermalization transition; data for larger n (darker shades) sharpen this crossover, consistent with the main-text diagnostics. Each point is obtained by averaging over 200 independent disorder realizations.

C Proof of Theorem 1

Proof Let $|\psi_{\text{in}}\rangle$ be an arbitrary n-qubit input state, and consider the parametrized quantum state $|\psi(\boldsymbol{\vartheta})\rangle = \hat{U}(\boldsymbol{\vartheta})|\psi_{\text{in}}\rangle$. Since the ensemble $\{\hat{U}(\boldsymbol{\vartheta})\}_{\vartheta\in\Theta}$ forms a unitary t-design, its t-fold moments reproduce those of the Haar measure. Consequently, for every basis vector $|\beta\rangle$, we have

$$\int_{\Theta} |\langle\beta|\psi(\boldsymbol{\vartheta})\rangle|^{2t} d\boldsymbol{\vartheta} = \mathbb{E}_{|\phi\rangle\sim\text{Haar}}\big[|\langle\beta|\phi\rangle|^{2t}\big]. \tag{45}$$

It is known that, for a Haar-random state $|\phi\rangle$, the moment on the right-hand side equals the inverse of the dimension of the totally symmetric subspace $\vee^t\mathbb{C}^{2^n}$ [70, 76]. Specifically,

$$\dim(\vee^t\mathbb{C}^{2^n}) = \binom{2^n+t-1}{t} \tag{46}$$

and

$$\begin{aligned}\mathbb{E}_{|\phi\rangle\sim\text{Haar}}\big[|\langle\beta|\phi\rangle|^{2t}\big] =& \mathbb{E}_{|\phi\rangle\sim\text{Haar}}\big[\langle\beta|^{\otimes t}|\phi\rangle^{\otimes t}\langle\phi|^{\otimes t}|\beta\rangle^{\otimes t}\big] \\ =& \langle\beta|^{\otimes t}\big[\mathbb{E}_{|\phi\rangle\sim\text{Haar}}\big(|\phi\rangle^{\otimes t}\langle\phi|^{\otimes t}\big)\big]|\beta\rangle^{\otimes t} \\ =& \frac{\langle\beta|^{\otimes t}\Pi_{\text{sym}}|\beta\rangle^{\otimes t}}{\dim\big(\vee^t\mathbb{C}^{2^n}\big)} \\ =& \frac{1}{\dim\big(\vee^t\mathbb{C}^{2^n}\big)},\end{aligned} \tag{47}$$

where Π_{sym} denotes the projector onto the totally symmetric subspace. Substituting this expression into Eq. (45) and summing over the complete computational basis $\{|\beta_j\rangle\}_{j=1}^{2^n}$ we obtain

$$\int_{\Theta} \text{IPR}_t(|\psi(\boldsymbol{\vartheta})\rangle) d\boldsymbol{\vartheta} = \frac{2^n}{\dim\big(\vee^t\mathbb{C}^{2^n}\big)} = \frac{2^n!\,t!}{(t+2^n-1)!}. \tag{48}$$

Setting $t = 2$ immediately yields

$$\dim(\vee^2\mathbb{C}^{2^n}) = \binom{2^n+1}{2} = \frac{2^n(2^n+1)}{2}. \tag{49}$$

Hence

$$\int_{\Theta} \text{IPR}_2(|\psi(\boldsymbol{\vartheta})\rangle) d\boldsymbol{\vartheta} = \frac{2}{(2^n+1)}. \tag{50}$$

■

D State 2-Design and Circuit Expressibility

As previously noted in Section 3, although the inverse participation ratio (IPR_t) can suggest whether a quantum state ensemble deviates from forming a t-design, it is not solely sufficient for such a determination. To provide further evidence that, in the thermal phase, the output-state ensemble approaches a state t-design (with respect to the Haar measure on pure states), we investigate the frame potential, defined for t-th order moments as:

$$\mathcal{F}_t = \int_{\Theta}\int_{\Theta} |\langle\psi(\boldsymbol{\vartheta}_1) \mid \psi(\boldsymbol{\vartheta}_2)\rangle|^{2t}\, d\boldsymbol{\vartheta}_1 d\boldsymbol{\vartheta}_2. \tag{51}$$

An ensemble qualifies as a state t-design if its frame potential matches the Haar measure frame potential, known as the Welch bounds:

$$\mathcal{F}_t = \mathcal{F}_t^{(\text{Haar})} := \frac{1}{\dim\big(\vee^t\mathbb{C}^{2^n}\big)} = \frac{1}{\binom{t+2^n-1}{t}}. \tag{52}$$

For a state 2-design in particular, this criterion simplifies to:

$$\mathcal{F}_2 = \mathcal{F}_2^{(\text{Haar})} := \frac{2}{2^n(2^n+1)}. \tag{53}$$

We calculate the average frame potentials $\mathcal{F}_2$, $\mathcal{F}_4$, and $\mathcal{F}_6$ across various values of W, and present these findings in Fig. 9 (a-f). In the thermal phase, these averaged frame potentials accurately reflect their theoretical Haar values, substantiating the ensemble's transition to state designs.

Additionally, the ratio between $\mathcal{F}_2$ and $\mathcal{F}_2^{(\text{Haar})}$ is indicative of the circuit's state-dependent expressibility [65], defined as:

$$\varepsilon_t(|\psi_t\rangle\langle\psi_t|) := \left\| \int_\Theta \hat{U}(\boldsymbol{\vartheta})^{\otimes t}(|\psi_t\rangle\langle\psi_t|^{\otimes t})\hat{U}^\dagger(\boldsymbol{\vartheta})^{\otimes t} d\boldsymbol{\vartheta} - \int_{\mathrm{U}(2^n)} \hat{U}^{\otimes t}(|\psi_t\rangle\langle\psi_t|^{\otimes t})\hat{U}^{\dagger\otimes t} d\mu_{\mathrm{H}}(\hat{U}) \right\|_2. \tag{54}$$

Here, our trial state $|\psi_t\rangle$ is sampled from the computational basis. Larger ratios suggest reduced expressibility of the ansatz, whereas ratios approaching 1 indicate maximal expressibility associated with strong barren plateaus. Fig. 9 (g) shows these ratios for the MBL phase ($W = \pi/10$) and the thermal phase ($W = 9\pi/20$) in the 1D ring topology, and Fig. 9 (h) for the MBL phase ($W = \pi/20$) and the thermal phase ($W = 9\pi/40$) in the $\mathrm{Ci}_n(1,2)$ lattice topology. In the MBL phase, these ratios exponentially increase with the system size n, indicating limited expressibility, whereas in the thermal phase, they remain constant near 1, indicative of maximal expressibility.

E Proof of Theorem 2

Throughout this appendix we denote $N = 2^n$ and always work with the $q := 2t$-th moment of overlaps.

Proof Let $\hat{O}$ be a traceless Hermitian operator with eigenvalues $\pm\lambda$. Choose an eigenbasis $\{|p_j\rangle, |m_j\rangle\}_{j=1}^{N/2}$ such that

$$\hat{O}|p_j\rangle = +\lambda|p_j\rangle, \tag{55}$$

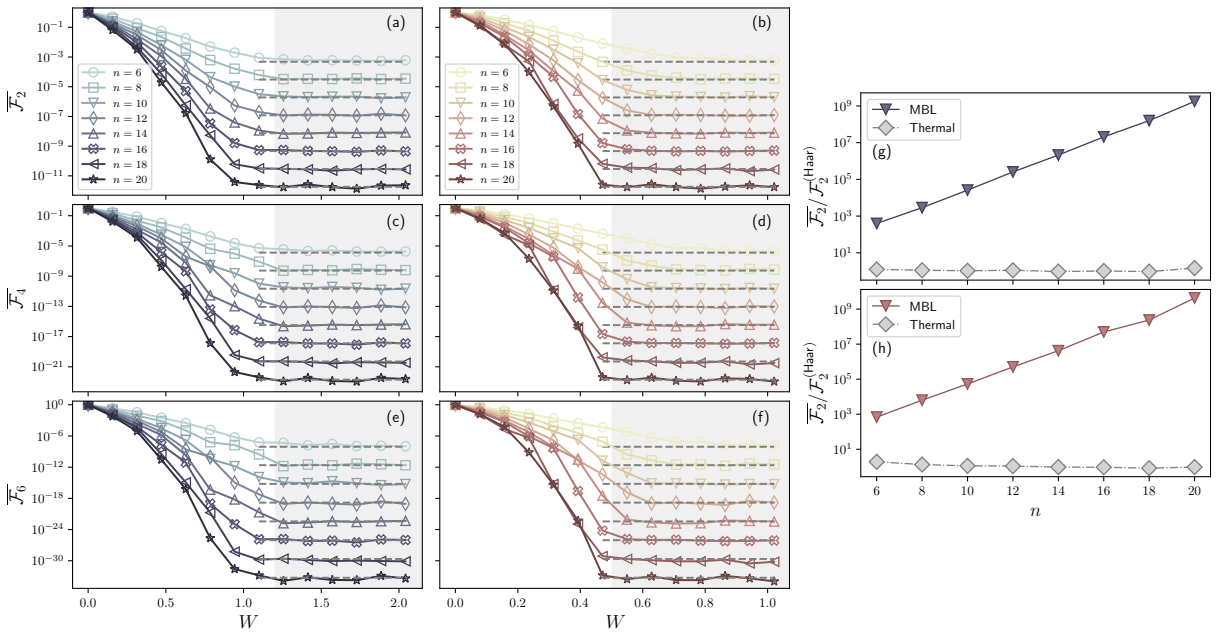


Figure 9: Frame potentials of output states across different orders as a function of kick strength W for various lattice topologies, demonstrating how close the ensembles approach state t-designs. **(a, c, e)** display results for the 1D ring topology. **(b, d, f)** show results for the $\mathrm{Ci}_n(1,2)$ lattice topology. Each panel presents frame potentials of different orders: **(a, b)** second-order, **(c, d)** fourth-order, and **(e, f)** sixth-order. Data averaged over 100 samples, with grey dashed lines indicating the Welch bounds [109]. **(g)** and **(h)** illustrate the ratios between the computed frame potentials and the corresponding Haar-random frame potentials for the 1D ring and the $\mathrm{Ci}_n(1,2)$ lattice, respectively.

and

$$\hat{O}|m_j\rangle = -\lambda|m_j\rangle. \tag{56}$$

For a pair of multi–indices $\boldsymbol{\alpha} = (\alpha_1, \ldots, \alpha_q) \in \{1, \ldots, N/2\}^q$ and $\boldsymbol{\sigma} = (\sigma_1, \ldots, \sigma_q) \in \{+1, -1\}^q$ define

$$|v_\ell\rangle := \begin{cases} |p_{\alpha_\ell}\rangle, & \sigma_\ell = +1, \\ |m_{\alpha_\ell}\rangle, & \sigma_\ell = -1, \end{cases} \quad \operatorname{sgn}(\boldsymbol{\sigma}) := \prod_{\ell=1}^{q} \sigma_\ell. \tag{57}$$

We say that a pair $(\boldsymbol{\alpha}, \boldsymbol{\sigma})$ is weakly ordered if the indices $\boldsymbol{\alpha}$ satisfy

$$\alpha_1 \le \alpha_2 \le \cdots \le \alpha_q. \tag{58}$$

For every weakly–ordered pair $(\boldsymbol{\alpha}, \boldsymbol{\sigma})$ put

$$\begin{aligned} \hat{Q}_{\boldsymbol{\alpha},\boldsymbol{\sigma}} :=& |v_1\rangle\langle v_1| \otimes \cdots \otimes |v_q\rangle\langle v_q|, \\ n_j :=& \big|\{\ell : \alpha_\ell = j\}\big|. \end{aligned} \tag{59}$$

Because the operator $\hat{O}^{\otimes q}$ is totally symmetric, the following weighted sum reproduces it exactly:

$$\hat{O}^{\otimes q} = \lambda^q \sum_{\substack{\text{weakly ordered} \\ (\boldsymbol{\alpha},\boldsymbol{\sigma})}} \frac{q!}{\prod_j n_j!} \operatorname{sgn}(\boldsymbol{\sigma}) \hat{Q}_{\boldsymbol{\alpha},\boldsymbol{\sigma}}, \tag{60}$$

To clarify the notation used in the proof, let's consider a simple example. Let our system be a single qubit ($n = 1$, so the Hilbert space dimension is $N = 2^1 = 2$) and let the operator be $\hat{O} = \hat{\sigma}_z$. The eigenvalues are $\lambda = \pm 1$. The corresponding eigenspaces, indexed by $j \in \{1, \ldots, N/2 = 1\}$, are spanned by:

- Positive eigenspace ($j = 1$): $|p_1\rangle = |0\rangle$ (for eigenvalue $+1$)
- Negative eigenspace ($j = 1$): $|m_1\rangle = |1\rangle$ (for eigenvalue -1)

We will examine the second moment, which corresponds to setting $t = 1$ and thus $q = 2t = 2$. The multi-index for the eigenspace, $\boldsymbol{\alpha} = (\alpha_1, \alpha_2)$, must be $(1, 1)$ since j can only be 1. The sign multi-index $\boldsymbol{\sigma} = (\sigma_1, \sigma_2)$ can vary, leading to different operators $\hat{Q}_{\boldsymbol{\alpha},\boldsymbol{\sigma}}$.

- **Case 1:** $\boldsymbol{\sigma} = (+, +)$
  - The state vectors are $|v_1\rangle = |p_1\rangle = |0\rangle$ and $|v_2\rangle = |p_1\rangle = |0\rangle$.
  - The operator is $\hat{Q}_{(1,1),(+,+)} = |0\rangle\langle 0| \otimes |0\rangle\langle 0| = |00\rangle\langle 00|$.
  - The sign contribution is $\operatorname{sgn}(\boldsymbol{\sigma}) = (+1)(+1) = +1$.
- **Case 2:** $\boldsymbol{\sigma} = (+, -)$
  - The state vectors are $|v_1\rangle = |p_1\rangle = |0\rangle$ and $|v_2\rangle = |m_1\rangle = |1\rangle$.
  - The operator is $\hat{Q}_{(1,1),(+,-)} = |0\rangle\langle 0| \otimes |1\rangle\langle 1| = |01\rangle\langle 01|$.
  - The sign contribution is $\operatorname{sgn}(\boldsymbol{\sigma}) = (+1)(-1) = -1$.

The other two cases, $\boldsymbol{\sigma} = (-, +)$ and $\boldsymbol{\sigma} = (-, -)$, are analogous. The full expansion of $(\hat{\sigma}_z)^{\otimes 2}$ is given by:

$$\begin{aligned} (\hat{\sigma}_z)^{\otimes 2} &= (|0\rangle\langle 0| - |1\rangle\langle 1|) \otimes (|0\rangle\langle 0| - |1\rangle\langle 1|) \\ &= |00\rangle\langle 00| - |01\rangle\langle 01| - |10\rangle\langle 10| + |11\rangle\langle 11| \end{aligned} \tag{61}$$

Let $|\psi\rangle$ be a Haar-random state on $\mathbb{C}^N$. Since

$$\mathbb{E}_\psi\big[|\psi\rangle\langle\psi|^{\otimes q}\big] = \frac{\Pi_{\text{sym}}}{\binom{N+q-1}{q}}, \tag{62}$$

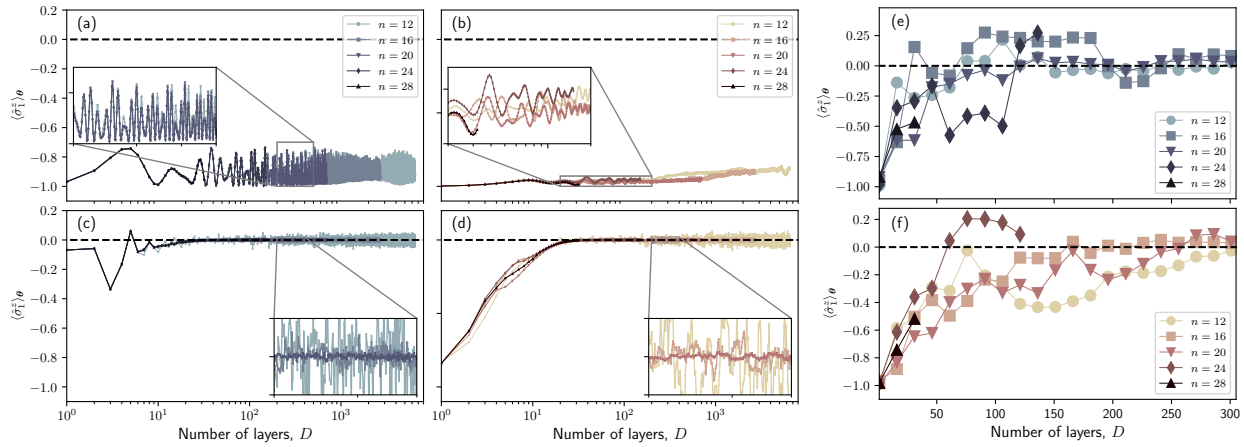


Figure 10: Demonstration of many-body localization within a circuit model, showcasing the output expectation values from deep variational quantum circuits across different phases and initializations. **(a, c)** Illustrate results for a 1D ring topology under MBL conditions with kick strengths $W = 1/5$ and $W = 7/5$ respectively, highlighting the preservation of local information even at greater circuit depths. **(b, d)** Display outcomes for a $\mathrm{Ci}_n(1, 2)$ lattice topology with kick strengths $W = 1/10$ and $W = 7/10$ respectively, reflecting the dynamics across both MBL and thermal phases. **(e, f)** Compare these with results from non-Floquet-initialized circuits for the same topologies but with each parameter independently sampled from narrow ranges $[-1/5, 1/5]$ and $[-1/10, 1/10]$, respectively. These panels demonstrate a rapid loss of local information within about 100 layers, starkly contrasting with the robustness observed in the Floquet-initialized systems depicted in panels (a-d).

with Π_{sym} the projector onto the totally symmetric subspace $\vee^q \mathbb{C}^N$, it follows that from (60)

$$\mathbb{E}_\psi\big[\langle\psi|\hat{O}|\psi\rangle^q\big] = \frac{\lambda^q}{\binom{N+q-1}{q}} \sum_{\substack{\text{weakly ordered} \\ (\boldsymbol{\alpha},\boldsymbol{\sigma})}} \frac{q!}{\prod_j n_j!} \operatorname{sgn}(\boldsymbol{\sigma}) \operatorname{Tr}\big(\Pi_{\mathrm{sym}} \hat{Q}_{\boldsymbol{\alpha},\boldsymbol{\sigma}}\big) \tag{63}$$

The overlap with Π_{sym} depends only on how many signs in $\boldsymbol{\sigma}$ are negative; a short combinatorial count yields

$$\mathbb{E}_\psi\big[\langle\psi|\hat{O}|\psi\rangle^q\big] = \lambda^q \frac{\binom{N/2+t-1}{t}}{\binom{N+q-1}{q}}. \tag{64}$$

For every non-identity Pauli $\hat{P} \in \mathcal{P}_{n,k} \setminus \{\mathbb{1}\}$ we have $\lambda = 1$. Replacing $|\psi\rangle$ by $|\psi(\boldsymbol{\vartheta})\rangle := \hat{U}(\boldsymbol{\vartheta})|\psi_{\mathrm{in}}\rangle$ and averaging over the unitary q-design $\{\hat{U}(\boldsymbol{\vartheta})\}_{\boldsymbol{\vartheta}\in\Theta}$ gives, by (64),

$$\int_\Theta \langle\psi(\boldsymbol{\vartheta})|\hat{P}|\psi(\boldsymbol{\vartheta})\rangle^q \mathrm{d}\boldsymbol{\vartheta} = \frac{\binom{N/2+t-1}{t}}{\binom{N+q-1}{q}}. \tag{65}$$

For the identity operator the same integral equals 1. Splitting the sum over the low-weight Pauli set $\mathcal{P}_{n,k}$ into identity plus $\mathrm{card}(\mathcal{P}_{n,k}) - 1$ traceless strings we arrive at

$$\begin{aligned} \int_\Theta \sum_{\hat{P}\in\mathcal{P}_{n,k}} \frac{|\langle\psi(\boldsymbol{\vartheta})|\hat{P}|\psi(\boldsymbol{\vartheta})\rangle|^q}{\mathrm{card}(\mathcal{P}_{n,k})} d\boldsymbol{\vartheta} &= \frac{1}{\mathrm{card}(\mathcal{P}_{n,k})} + \frac{(\mathrm{card}(\mathcal{P}_{n,k}) - 1)}{\mathrm{card}(\mathcal{P}_{n,k})} \frac{\binom{2^{n-1}+q/2-1}{q/2}}{\binom{2^n+q-1}{q}} \\ &= \frac{\binom{2^n+q-1}{q} - \binom{2^{n-1}+q/2-1}{q/2}}{\mathrm{card}(\mathcal{P}_{n,k})\binom{2^n+q-1}{q}} + \frac{\binom{2^{n-1}+q/2-1}{q/2}}{\binom{2^n+q-1}{q}}. \end{aligned} \tag{66}$$

■

F Dynamics of Deep Circuits

In this section, we employ our Floquet initialization strategy while substantially extending the circuit depth to investigate the dynamics of deep quantum circuits. We examine the output expectation values of Pauli $\hat{\sigma}_j^z$ on the first qubit over a range of circuit depths D. We utilize both many-body localization (MBL) and thermal initializations to explore their distinct dynamics. Specifically, we apply a kick strength of $W = 0.2$ for the 1D ring topology and $W = 0.1$ for the $\mathrm{Ci}_n(1,2)$ lattice topology under MBL conditions, and set the strengths to $W = 1.4$ for the 1D ring and $W = 0.7$ for the $\mathrm{Ci}_n(1,2)$ under thermal conditions. The results are illustrated in Fig. 10(a-d). Remarkably, the local information in the MBL phase remains robustly preserved even beyond 1000 layers, underscoring the effectiveness of MBL dynamics in protecting initial system information within extremely deep circuits. This preservation sharply contrasts with the outcomes from circuits without Floquet initialization, where local information typically diminishes as circuit depth increases. We provide a comparative analysis by showing results from circuits with non-Floquet initialization, where each parameter is independently sampled from a narrow range of $[-0.2, 0.2]$ for the 1D ring and $[-0.1, 0.1]$ for the $\mathrm{Ci}_n(1,2)$ lattice. The results, depicted in Fig. 10(e,f), demonstrate that the initial local information is entirely lost after approximately 100 iterations. Despite significant fluctuations observed over extended periods, the MBL phase distinctly demonstrates its capacity to mitigate the loss of local information, reflecting the characteristic resilience of standard many-body localized systems.

Without loss of generality, we focus on the fluctuations of the output expectation values for circuit depths D ranging from 500 to 1500, using $N = 1000$ data points in a 16-qubit system. Initially, we apply linear regression to detrend the original data:

$$y_D = \langle \hat{\sigma}_1^z \rangle_D - \overline{\langle \hat{\sigma}_1^z \rangle} - f(D), \tag{67}$$

where $f(D)$ represents the linear regression function fitted to the data. To mitigate spectral leakage in the power spectral density (PSD) analysis [110], we employ a window function:

$$\tilde{y}_D = y_D \cdot w_D, \tag{68}$$

where w_D is the Hanning window, defined as:

$$w_D = \frac{1}{2}\left(1 - \cos\left(\frac{2\pi D}{N-1}\right)\right). \tag{69}$$

Subsequently, we calculate the discrete Fourier transform of the windowed data using the fast Fourier transform algorithm:

$$z_k = \sum_{D=0}^{N-1} \tilde{y}_D \cdot e^{-i\frac{2\pi k D}{N}}, \tag{70}$$

where z_k represents the k-th element of the Fourier transform. The PSD, PSD_k, is determined by taking the square of the absolute value of z_k and normalizing by the number of data points:

$$\mathrm{PSD}_k = \frac{|z_k|^2}{N}. \tag{71}$$

The PSD is then normalized by dividing each element by the total power, which is the sum of all PSD values:

$$\widetilde{\mathrm{PSD}}_k = \frac{\mathrm{PSD}_k}{\sum_{j=0}^{N/2} \mathrm{PSD}_j}. \tag{72}$$

The resulting normalized spectrum, $\widetilde{\mathrm{PSD}}_k$, illustrated in Fig. 11, reveals distinct characteristics of the circuit dynamics across different phases. In the MBL phase, the power spectrum displays several prominent peaks, indicative of multiple dominant frequency components. This suggests that the circuit's dynamical evolution is characterized by various periodic patterns with distinct frequencies.

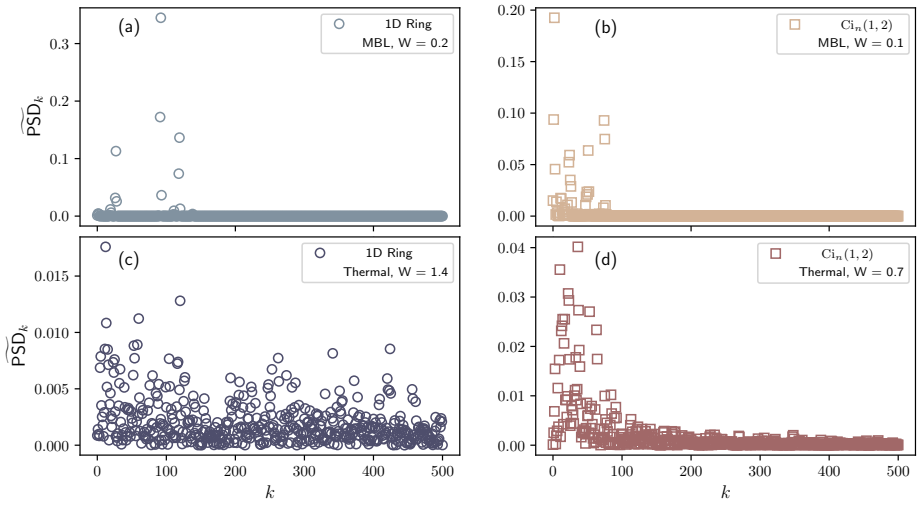


Figure 11: Power spectrum analysis of the output state expectation value fluctuations for $\hat{\sigma}_1^z$ in a 16-qubit system, with circuit depth D varying from 100 to 500. This analysis continues using our Floquet initialization strategy, extending the circuit depth significantly. Panels **(a, c)** illustrate results for a 1D ring topology with kick strengths $W = 0.2, 1.4$, respectively; panels **(b, d)** display the $\mathrm{Ci}_n(1,2)$ lattice topology with kick strengths $W = 0.1, 0.7$, respectively.

Conversely, in the thermal phase, the power spectrum exhibits a more uniform distribution of frequencies with fewer dominant components. This notable difference in spectral characteristics between the MBL and thermal phases provides a compelling diagnostic tool for characterizing and distinguishing the dynamical behavior of variational quantum circuits in different operational phases.

G Connecting the Gradient's ℓ_∞-Norm to Component Variance

Proposition 2 *Let $\boldsymbol{\vartheta} \in \mathbb{R}^{D(m_s+m_k)}$ be drawn from a distribution $\mathcal{D}$, and denote the gradient of the expectation value of the loss Hamiltonian by*

$$\nabla\langle\hat{\mathcal{H}}\rangle_{\boldsymbol{\vartheta}} = (\partial_{\vartheta_1}\langle\hat{\mathcal{H}}\rangle_{\boldsymbol{\vartheta}}, \ldots, \partial_{\vartheta_{D(m_s+m_k)}}\langle\hat{\mathcal{H}}\rangle_{\boldsymbol{\vartheta}}). \tag{73}$$

Assume the gradient vanishes on average, a standard premise in the analysis of barren plateaus:

$$\mathbb{E}_{\boldsymbol{\vartheta}\sim\mathcal{D}}[\nabla\langle\hat{\mathcal{H}}\rangle_{\boldsymbol{\vartheta}}] = \mathbf{0}. \tag{74}$$

If there exist constants $\alpha, p > 0$ such that

$$\Pr_{\boldsymbol{\vartheta}\sim\mathcal{D}}\left[\|\nabla\langle\hat{\mathcal{H}}\rangle_{\boldsymbol{\vartheta}}\|_\infty \geq \alpha\right] \geq p, \tag{75}$$

then there exists at least one component $j \in \{1, \ldots, D(m_s + m_k)\}$ such that

$$\mathrm{Var}_{\boldsymbol{\vartheta}\sim\mathcal{D}}\left[\partial_{\vartheta_j}\langle\hat{\mathcal{H}}\rangle_{\boldsymbol{\vartheta}}\right] \geq \frac{p\alpha^2}{D(m_s+m_k)}. \tag{76}$$

In particular, if both p and α scale inverse-polynomially with the number of qubits n, the gradient variance cannot decay faster than polynomially in n, ruling out exponential barren-plateau behavior.

Proof Since $\mathbb{E}_{\mathcal{D}}[\nabla\langle\hat{\mathcal{H}}\rangle_{\boldsymbol{\vartheta}}] = \mathbf{0}$, we have

$$\mathrm{Var}_{\mathcal{D}}\left[\partial_{\vartheta_j}\langle\hat{\mathcal{H}}\rangle_{\boldsymbol{\vartheta}}\right] = \mathbb{E}_{\mathcal{D}}\left[\left(\partial_{\vartheta_j}\langle\hat{\mathcal{H}}\rangle_{\boldsymbol{\vartheta}}\right)^2\right]. \tag{77}$$

Whenever $\|\nabla\langle\hat{\mathcal{H}}\rangle_{\boldsymbol{\vartheta}}\|_\infty \geq \alpha$, there exists some k such that $(\partial_{\vartheta_k}\langle\hat{\mathcal{H}}\rangle_{\boldsymbol{\vartheta}})^2 \geq \alpha^2$. This implies

$$\sum_{i=1}^{D(m_s+m_k)} (\partial_{\vartheta_i}\langle\hat{\mathcal{H}}\rangle_{\boldsymbol{\vartheta}})^2 \geq \alpha^2. \tag{78}$$

Taking expectations,

$$\sum_{i=1}^{D(m_s+m_k)} \mathrm{Var}_{\mathcal{D}}\left[\partial_{\vartheta_i}\langle\hat{\mathcal{H}}\rangle_{\boldsymbol{\vartheta}}\right] = \mathbb{E}_{\mathcal{D}}\left[\|\nabla\langle\hat{\mathcal{H}}\rangle_{\boldsymbol{\vartheta}}\|_2^2\right] \geq p\alpha^2, \tag{79}$$

so at least one term in the sum must satisfy the lower bound claimed. ■

For the Floquet-initialized parameter ensemble used in this work, kick angles are drawn from intervals symmetric about zero, and steady angles uniformly from $[-\pi, \pi)$. Combined with the parity properties of $\langle\hat{\mathcal{H}}\rangle_{\boldsymbol{\vartheta}}$, this ensures that $\mathbb{E}_{\mathcal{D}}[\nabla\langle\hat{\mathcal{H}}\rangle_{\boldsymbol{\vartheta}}] = \mathbf{0}$, satisfying the premise of Proposition 2. Therefore, the observed inverse-polynomial lower bound on $\|\nabla\langle\hat{\mathcal{H}}\rangle_{\boldsymbol{\vartheta}}\|_\infty$ (see Fig. 3) directly implies an inverse-polynomial lower bound on the gradient variance, reconciling our results with the standard variance-based barren plateau framework.

H Proof of Theorem 3

Proof Let $\boldsymbol{\delta} := \boldsymbol{\vartheta}_{\mathrm{th}} - \boldsymbol{\vartheta}_{\mathrm{MBL}}$, and define the linear path

$$\gamma(s) := (1-s)\boldsymbol{\vartheta}_{\mathrm{MBL}} + s\boldsymbol{\vartheta}_{\mathrm{th}}, \quad s \in [0,1]. \tag{80}$$

By the chain rule,

$$\frac{d}{ds}\langle\hat{\mathcal{H}}\rangle_{\gamma(s)} = \nabla_{\boldsymbol{\vartheta}}\langle\hat{\mathcal{H}}\rangle_{\gamma(s)} \cdot \boldsymbol{\delta}. \tag{81}$$

Integrating both sides over $s \in [0,1]$ and applying the triangle inequality yields

$$\left|\langle\hat{\mathcal{H}}\rangle_{\boldsymbol{\vartheta}_{\mathrm{th}}} - \langle\hat{\mathcal{H}}\rangle_{\boldsymbol{\vartheta}_{\mathrm{MBL}}}\right| \leq \int_0^1 \left|\nabla_{\boldsymbol{\vartheta}}\langle\hat{\mathcal{H}}\rangle_{\gamma(s)} \cdot \boldsymbol{\delta}\right| ds. \tag{82}$$

Applying Hölder's inequality,

$$\left|\nabla_{\boldsymbol{\vartheta}}\langle\hat{\mathcal{H}}\rangle_{\gamma(s)} \cdot \boldsymbol{\delta}\right| \leq \left\|\nabla_{\boldsymbol{\vartheta}}\langle\hat{\mathcal{H}}\rangle_{\gamma(s)}\right\|_\infty \cdot \|\boldsymbol{\delta}\|_1, \tag{83}$$

we obtain

$$\left|\langle\hat{\mathcal{H}}\rangle_{\boldsymbol{\vartheta}_{\mathrm{th}}} - \langle\hat{\mathcal{H}}\rangle_{\boldsymbol{\vartheta}_{\mathrm{MBL}}}\right| \leq \|\boldsymbol{\delta}\|_1 \cdot \mathbb{E}_{s\in[0,1]}\left\|\nabla_{\boldsymbol{\vartheta}}\langle\hat{\mathcal{H}}\rangle_{\gamma(s)}\right\|_\infty. \tag{84}$$

Now we bound $\|\boldsymbol{\delta}\|_1$. By uniform kick scaling, each of the Dm_k kick parameters is multiplied by a factor $\lambda > 1$, and satisfies

$$|\delta^{(\ell,j)}| = (\lambda-1)|\vartheta^{(1,j)}_{\mathrm{MBL}}| \leq (\lambda-1)W, \tag{85}$$

since the kick parameters in $\boldsymbol{\vartheta}_{\mathrm{MBL}}$ lie in $[-W, W]$. Therefore,

$$\|\boldsymbol{\delta}\|_1 \leq Dm_k(\lambda-1)W. \tag{86}$$

Substituting (86) into (84), and dividing both sides by $Dm_k(\lambda-1)W$, we obtain

$$\mathbb{E}_{s\in[0,1]}\left\|\nabla_{\boldsymbol{\vartheta}}\langle\hat{\mathcal{H}}\rangle_{\gamma(s)}\right\|_\infty \gtrsim \frac{\left|\langle\hat{\mathcal{H}}\rangle_{\boldsymbol{\vartheta}_{\mathrm{MBL}}} - \langle\hat{\mathcal{H}}\rangle_{\boldsymbol{\vartheta}_{\mathrm{th}}}\right|}{Dm_k(\lambda-1)W}. \tag{87}$$

Under the assumption that $\langle\hat{\mathcal{H}}\rangle_{\boldsymbol{\vartheta}_{\mathrm{MBL}}} = \Theta(1)$ and $\langle\hat{\mathcal{H}}\rangle_{\boldsymbol{\vartheta}_{\mathrm{th}}}$ is exponentially small in n, the numerator is $\Theta(1)$, while the denominator grows at most polynomially in n, since $D, m_k = \mathrm{poly}(n)$. This establishes that the average gradient norm remains inverse-polynomial in n, completing the proof. ■

I Additional Benchmarks and Robustness Tests

To evaluate the robustness of our approach, we analyze a more complex system characterized by the following Hamiltonian:

$$\hat{\mathcal{H}} = \sum_{i<j} \frac{J[1+\gamma(-1)^{i+j}]}{2|i-j|^{\alpha}} (\hat{\sigma}_i^x \hat{\sigma}_j^x + \hat{\sigma}_i^y \hat{\sigma}_j^y + \Delta \hat{\sigma}_i^z \hat{\sigma}_j^z) + \sum_i h_i \hat{\sigma}_i^z. \tag{88}$$

This Hamiltonian describes a one-dimensional spin-1/2 chain with long-range power-law-decaying interactions (controlled by the exponent α), staggered couplings modulated by γ (where $0 \leq \gamma \leq 1$; $\gamma = 1$ implies couplings only at even distances, while $\gamma = 0$ removes staggering), anisotropy parameter Δ, and on-site magnetic fields h_i. For small values of α (e.g., $\alpha < 1.5$), the long-range interactions induce extended correlations that challenge classical tensor-network methods like density matrix renormalization group (DMRG) [59, 111], as they lead to rapid entanglement growth and require exponentially large bond dimensions for accurate approximations. In contrast, larger α (e.g., $\alpha \geq 2$) effectively reduces to short-range behavior, where DMRG performs efficiently.

To assess the limitations of classical MPS approximations, we first optimize MPS trial states with varying maximum bond dimensions χ, comparing the achieved energies to the exact ground-state energy. We fix $J = 1.0$. The results are shown in Fig. 12, where panels (a)-(c) correspond to fixed $\gamma = 3/4$, $\Delta = 2$, alternating fields $h_i = (-1)^i/2$, and panels (d)-(f) to sampled $\gamma \sim \text{Unif}(0.5, 1.0)$, $\Delta \sim \text{Unif}(1.0, 3.0)$, random fields with each h_i independently sampled uniformly from $[-1, 1]$ (averaged over 10 independent disorder realizations). Panels (a,d) use $\alpha = 1.1$, (b,e) $\alpha = 1.5$, and (c,f) $\alpha = 2.0$. In each subplot, the horizontal axis denotes the maximum bond dimension χ, and the vertical axis shows the absolute energy error $|\langle\hat{\mathcal{H}}\rangle_{\text{MPS}} - E_{\text{gs}}|$, for system sizes $n = 8, 12, 16, 20, 24, 28$. As expected, larger system sizes require higher χ for achieving a target accuracy, with the effect being more pronounced at smaller α (e.g., $\alpha = 1.1$), where long-range interactions degrade MPS performance.

Next, we compare the performance of our MBL-based initialization protocol against close-to-identity initialization, whose philosophy has been applied to achieve larger gradients [29, 36, 64], a common warm-start strategy in variational quantum algorithms that initializes circuit parameters near zero to preserve large gradients and proximity to the trial state. To evaluate their robustness against local minima, we employ the same hardware-efficient square circuit architecture (depth $D = n$) used

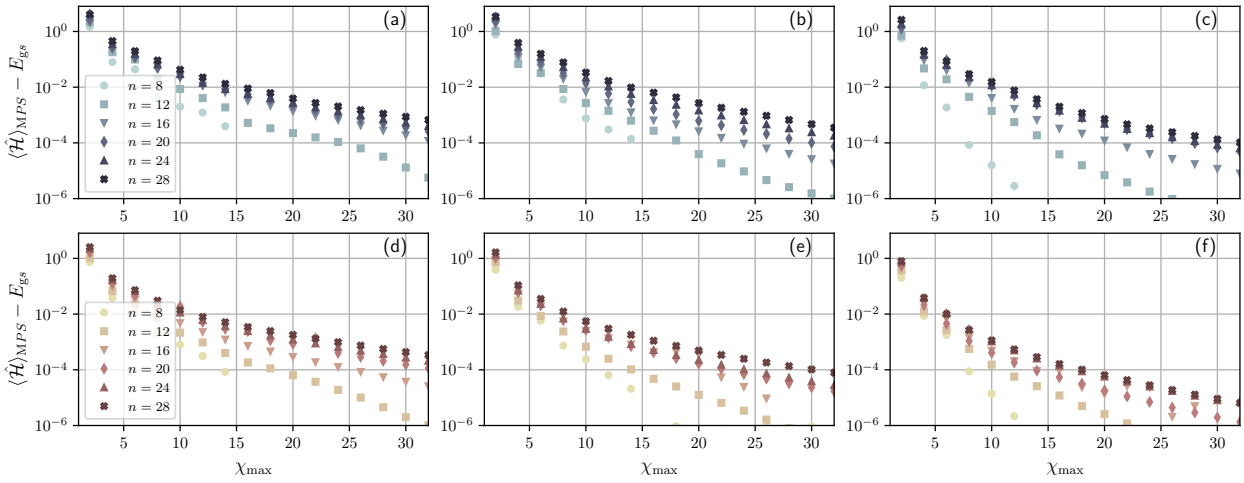


Figure 12: The absolute energy error relative to the exact ground state of MPS approximations for the long-range spin-chain Hamiltonian as a function of maximum bond dimension χ. Panels (a)-(c) show results for fixed $\gamma = 3/4$, $\Delta = 2$, alternating magnetic fields $h_i = (-1)^i/2$, while (d)-(f) correspond to sampled $\gamma \sim \text{Unif}(0.5, 1.0)$, $\Delta \sim \text{Unif}(1.0, 3.0)$, random fields h_i uniformly sampled from $[-1, 1]$ (averaged over 10 independent disorder realizations). Subpanels are organized by interaction decay exponent: (a,d) $\alpha = 1.1$ (strong long-range), (b,e) $\alpha = 1.5$ (intermediate), and (c,f) $\alpha = 2.0$ (effectively short-range). Each curve represents a different system size $n = 8, 12, 16, 20, 24, 28$, with darker shades indicating larger n.

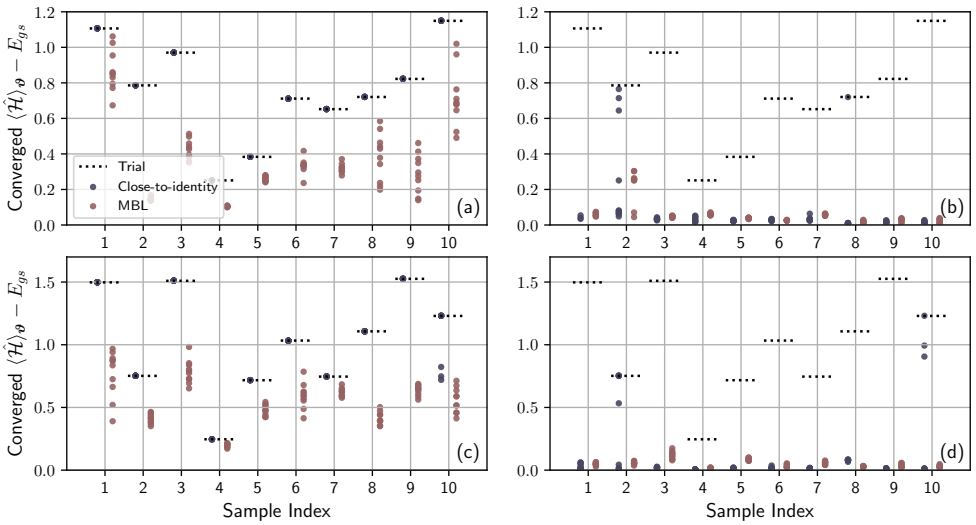


Figure 13: Comparison of converged energy errors for MBL initialization ($W = 0.2$) versus close-to-identity initialization (parameters sampled from $[-0.001, 0.001]$) across 10 random Hamiltonian instances. Each bar represents the absolute energy error $|\langle\hat{\mathcal{H}}\rangle - E_{\text{gs}}|$ for a single instance, with dashed lines indicating the trial-state energy error. Panels (a) and (b) show results for $n = 12$, while (c) and (d) are for $n = 16$. Standard gradient descent is used in (a) and (c), and the Adam optimizer in (b) and (d). Close-to-identity initialization (blue circles) often remains trapped near the trial energy, whereas MBL initialization (red circles) more reliably reaches lower energies.

throughout this work, along with an optimized MPS trial state with bond dimension $\chi = 2$. For close-to-identity initialization, all circuit parameters across all layers are independently and uniformly sampled from $[-0.001, 0.001]$. For MBL initialization, we set $W = 0.2$. Optimization proceeds via gradient descent until the energy fails to decrease by 10^{-4} over 50 consecutive iterations or reaches 1000 total iterations, at which point we record the final energy error relative to the exact ground state.

The results are presented in Fig. 13 for 10 independent random instances of the target Hamiltonian per subplot, with parameters sampled as follows: $\alpha \sim \text{Unif}(1, 2)$, $\gamma \sim \text{Unif}(0.5, 1.0)$, $\Delta \sim \text{Unif}(1.0, 3.0)$, $J = 1.0$, and on-site fields $h_i \sim \text{Unif}(-1, 1)$. Panels (a) and (c) show results for $n = 12$ and $n = 16$ using standard gradient descent, while (b) and (d) employ the Adam optimizer [112] with hyperparameters $\beta_1 = 0.9$, $\beta_2 = 0.999$ and a fixed learning rate of 0.005. In panels (a) and (c), close-to-identity initialization frequently converges to the trial-state energy, indicating entrapment in local minima near the initial point. In contrast, MBL initialization often escapes these minima, achieving substantially lower energies due to its sampling of a broader parameter space while remaining in a low-entanglement regime. Panels (b) and (d) demonstrate improved performance for both methods with Adam, which better navigates the optimization landscape; however, several close-to-identity instances still fail to escape local minima, whereas MBL consistently reaches lower energies for these samples. These findings do not imply an unconditional advantage for MBL initialization but highlight scenarios where its structured exploration of parameter space facilitates escape from trial-state-induced local minima, enhancing robustness for challenging long-range models.

To investigate the sensitivity of our MBL-initialized protocol to the quality of the trial state and the impact of finite-shot noise in energy estimation, we conduct additional numerical experiments on the long-range spin-chain Hamiltonian. We consider three types of bond-dimension-2 MPS trial states: (i) an optimized MPS obtained via DMRG, (ii) a perturbed version of this optimized MPS, where its tensor parameters are interpolated towards a random MPS with a small interpolation factor $\gamma_{\text{interp}} = 0.05$ (representing mild errors in trial-state preparation), and (iii) a fully random MPS ($\gamma_{\text{interp}} = 1$), which serves as a poor-quality baseline. The interpolation is performed as $\theta_{\text{interp}} = (1 - \gamma_{\text{interp}})\theta_{\text{opt}} + \gamma_{\text{interp}}\theta_{\text{rand}}$, where θ_{opt} and θ_{rand} are the tensor parameters of the optimized and random MPS, respectively. For each trial state, we apply the MBL-initialized variational circuit (depth $D = n = 12$, $W = 0.2$) and optimize using gradient descent with a step size of 0.005.

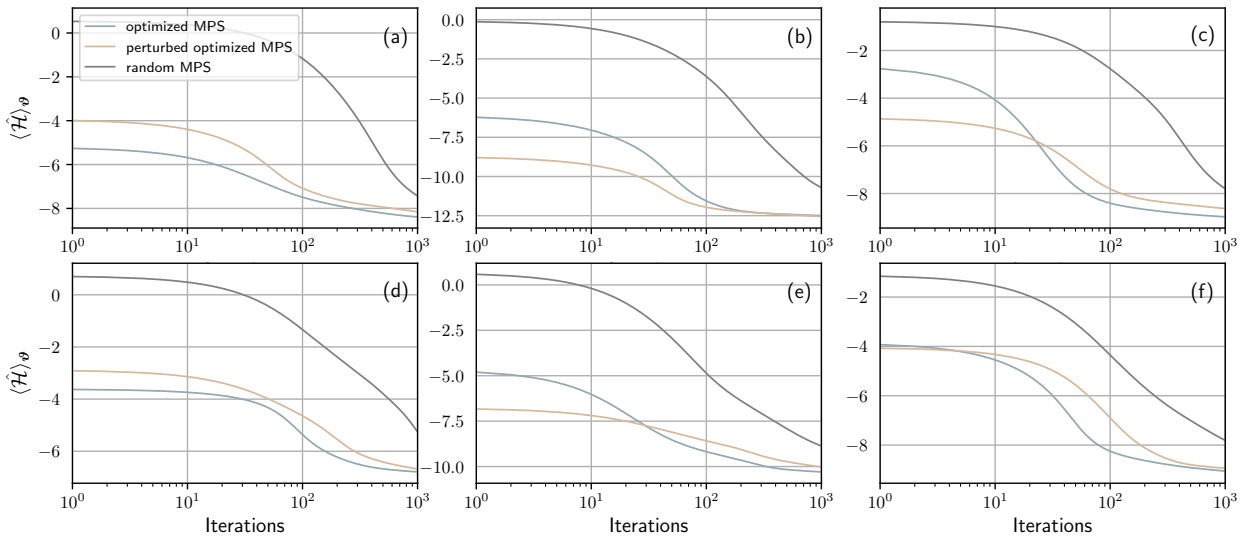


Figure 14: Optimization trajectories for the long-range spin-chain Hamiltonian ($n = 12$) under MBL initialization, showing sensitivity to trial-state quality and finite-shot effects across six independent Hamiltonian instances (panels a-f). Each panel displays three curves: optimized bond-2 MPS trial (blue), perturbed MPS ($\gamma_{\text{interp}} = 0.05$; brown), and random MPS ($\gamma_{\text{interp}} = 1$; gray). Solid lines denote exact (infinite-shot) energies, while shaded bands represent the mean ± standard deviation from 10 finite-shot repetitions (2048 shots per evaluation, with Pauli grouping and variance-based allocation).

Energy expectations during optimization are estimated using finite shots, incorporating Pauli grouping [113, 114] to reduce measurement overhead by simultaneously measuring commuting Pauli terms. Shot allocation is optimized adaptively based on the variance of each grouped observable. Specifically, for a Hamiltonian decomposed as $\hat{\mathcal{H}} = \sum_k c_k \hat{P}_k$ with $\hat{P}_k$ Pauli strings grouped into G commuting sets, the total variance of the estimator is bounded by $\mathrm{Var}(\langle\hat{\mathcal{H}}\rangle) \leq \sum_{g=1}^{G} (\sum_{k\in g} |c_k| \sqrt{\mathrm{Var}(\hat{P}_k)})^2 / S_g$, where S_g is the number of shots allocated to group g. We use 2048 shots per evaluation, distributed proportionally to the group variances to minimize the overall estimator variance, with the allocation recomputed every 10 iterations.

The optimization trajectories are shown in Fig. 14 for six independent Hamiltonian instances (sampled as $\alpha \sim \mathrm{Unif}(1, 2)$, $\gamma \sim \mathrm{Unif}(0.5, 1.0)$, $\Delta \sim \mathrm{Unif}(1.0, 3.0)$, $J = 1.0$, $h_i \sim \mathrm{Unif}(-1, 1)$), each in a separate panel (a)-(f). In each subplot, the three curves correspond to the optimized MPS trial (blue), perturbed MPS (orange), and random MPS (gray). Solid lines represent exact (infinite-shot) energies, while shaded bands indicate the mean ± one standard deviation from 10 repeated finite-shot evaluations at each step. Mild perturbations ($\gamma_{\text{interp}} = 0.05$) have minimal impact on convergence, with final energies closely matching those from the optimized trial. In contrast, fully random trials always lead to slower convergence and higher final errors, underscoring the importance of a reasonable initial approximation. Finite-shot noise introduces fluctuations, but with only 2048 shots, the estimates remain sufficiently accurate for guiding optimization, as the shot-induced variance scales as $\mathcal{O}(\|\hat{\mathcal{H}}\|^2/S)$ (where S is the total shots) and is independent of system size for Hamiltonians with bounded-norm terms. This independence arises because the estimator variance for a k-local Hamiltonian is bounded by $\mathcal{O}(\|\hat{\mathcal{H}}\|^2/S)$, where $\|\hat{\mathcal{H}}\|$ grows polynomially with n but can be mitigated through grouping and allocation without exponential overhead.

These results demonstrate that the MBL protocol exhibits robustness to moderate errors in the trial state, allowing for imperfect classical approximations without significant degradation. Moreover, the low shot requirements confirm practical viability on noisy intermediate-scale quantum devices, where measurement budgets are limited.